ACS OMEGA

Open Access

http://pubs.acs.org/journal/acsodf

Article

Triggering Breast Cancer Apoptosis via Cyclin-Dependent Kinase Inhibition and DNA Damage by Novel Pyrimidinone and 1,2,4-Triazolo[4,3-*a*]pyrimidinone Derivatives

Mohamed N. Abd Al Moaty, Yeldez El Kilany, Laila F. Awad,* Saied M. Soliman, Assem Barakat,* Nihal A. Ibrahim, Marwa M. Abu-Serie, Matti Haukka, Amira El-Yazbi, and Mohamed Teleb

Cite This: *ACS Omega* 2024, 9, 21042−21057

Read Online

ACCESS | Metrics & More | Article Recommendations | Supporting Information

ABSTRACT: Combinations of apoptotic inducers are common clinical practice in breast cancer. However, their efficacy is limited by the heterogeneous pharmacokinetic profiles. An advantageous alternative is merging their molecular entities in hybrid multitargeted scaffolds exhibiting synergistic activities and uniform distribution. Herein, we report apoptotic inducers simultaneously targeting DNA and CDK-2 (cyclin-dependent kinase-2) inspired by studies revealing that CDK-2 inhibition sensitizes breast cancer to DNA-damaging agents. Accordingly, rationally substituted pyrimidines and triazolopyrimidines were synthesized and assayed by MTT against MCF-7, MDA-MB231, and Wi-38 cells compared to doxorubicin. The *N*-(4-amino-2-((2-hydrazinyl-2-oxoethyl)-thio)-6-oxo-1,6-dihydropyrimidin-5-yl)acetamide **5** and its p-nitrophenylhydrazone **8** were the study hits against MCF-7 (IC_{50} = 0.050 and 0.146 μM) and MDA-MB231 (IC_{50} = 0.826 and 0.583 μM), induced DNA damage at 10.64 and 30.03 nM, and inhibited CDK-2 (IC_{50} = 0.172 and 0.189 μM). **5** induced MCF-7 apoptosis by 46.75% and disrupted cell cycle during S phase. Docking and MD simulations postulated their stable key interactions.

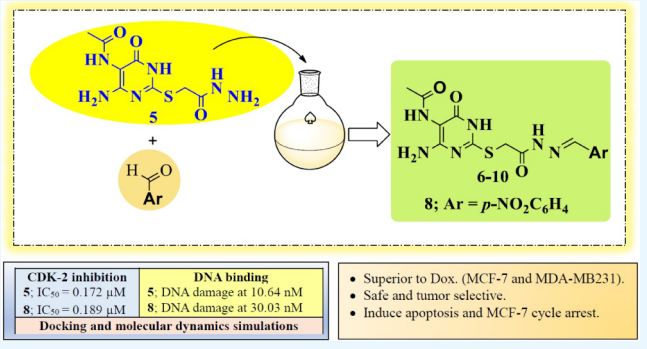

1. INTRODUCTION

Breast cancer continues to be the second cause of women death worldwide[1,2] with expectations that the number of patients will be doubled by 2030.[3,4] The severe adverse effects and prolonged sequelae of conventional breast cancer chemotherapy necessitate continuous development of new treatments. Besides, the growing knowledge of breast cancer molecular complexity and the acquired resistance mechanisms declares that it is almost impossible to achieve the desired therapeutic goals with single-drug treatment strategy.[5,6] Combination regimens have thus become common in the clinical practice of breast cancer management.[7] However, the combined agents remain different molecular entities with heterogeneous pharmacokinetic profiles, especially biodistribution. An advantageous alternative strategy is designing hybrid multitargeted agents combining the main pharmacophores of the required active entities into a single scaffold exhibiting synergistic activities and uniform distribution.[8] In breast cancer research, promising therapeutic outcomes were accomplished by synergistic induction of breast cancer apoptosis via targeting several molecular mediators of the pathway.[9] Along these lines, several studies utilized DNA-damaging agents as a main component of these apoptosis inducer regimens.[9] Since the first report elucidating the double-stranded DNA structure by Watson, Crick, and Wilkins in 1953,[10] DNA has been viewed as molecular target for halting carcinogenesis. Successive drug discovery studies employing molecular modeling introduced DNA intercalators that were advanced to clinical use.[11] Nevertheless, antibiotics research led to identifying the DNA-binding anthracycline doxorubicin,[12] the most frequently used chemotherapy in breast cancer that inhibits DNA synthesis through intercalation. Continuous progress led to a plethora of small molecules targeting DNA[13−15] mirrored by mechanistic studies underlying the cellular response to the induced DNA damage. In this regard, cyclin-dependent kinases, a family of serine/threonine kinases controlling cell cycle progression and DNA synthesis, received considerable attention with a special focus on CDK-2.[16] Combination studies revealed that inhibitors of CDK-2 can be applied to selectively enhance the therapeutic responses of breast cancer cells to DNA-damaging agents. Herein, CDK2 inhibition in MCF7 cells lead to delayed damage signaling through Rad51, Chk1, and p53 that coincided with an observed

Received: January 15, 2024
Revised: April 22, 2024
Accepted: April 24, 2024
Published: May 6, 2024

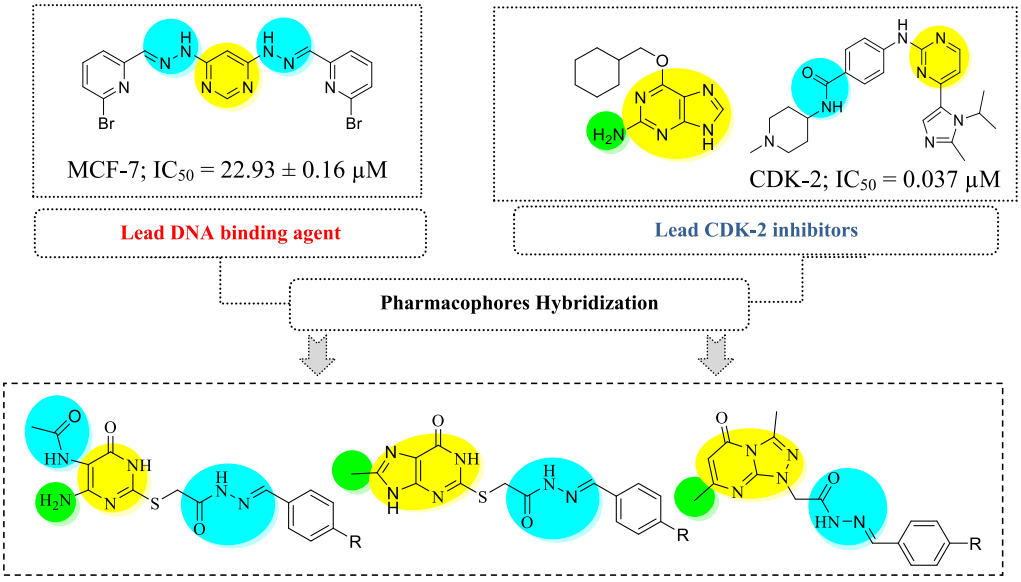

Figure 1. Lead DNA intercalators, CDK-2 inhibitors and the target pyrimidines, and 1,2,4-triazolo[4,3-*a*]pyrimidines.

Scheme 1. Synthesis of Substituted 5-Acetamido-4-amino-6-oxo-1,6-dihydropyrimidin-2-yl *S*-acyl Hydrazones 6−10

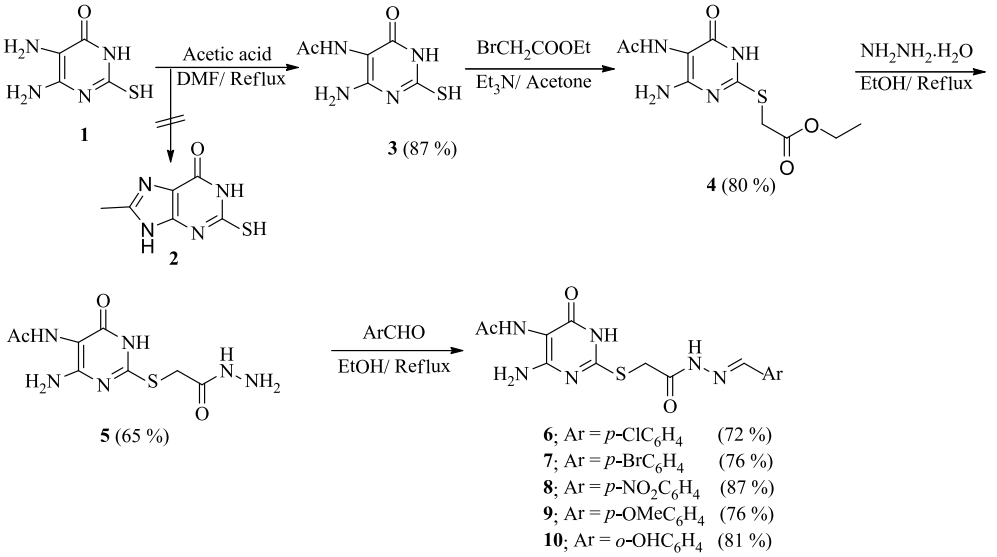

deficiency in DNA repair.[16] Already, flavopiridol, an inhibitor of multiple CDKs, has been raised to stage III clinical trials in combination with ionizing radiation.[17] Roscovitine, an inhibitor of CDK-2, 7, and 9, synergizes with radiation and caffeine, the ATM/ATR inhibitor, to induce cell killing in various tumors including breast cancer.[18,19] Indeed, the validity of CDK-2 as anticancer target was investigated by CDK-2 knockdown experiments in which CDK-2 loss failed to arrest the cell cycle in various tumor cell lines.[20] Such approach directed various drug discovery programs to develop optimized CDK-2 inhibitors as efficient anticancer agents.[21,22] Moreover, applying the therapeutic rationale outlined above, CDK-2 inhibitors are expected to have additional utility in settings in which the cancer is susceptible to DNA damage. Taken together, this study aims to structure optimization of novel DNA-binding agents endowed with intrinsic complementary CDK-2 inhibition for halting breast cancer progression. Such polypharmacology strategy is intended to augment the apoptotic induction capacity of DNA damage through concomitant CDK-2 inhibition by rationally designed dual mechanism hybrid molecules.

2. RATIONAL DESIGN

The dual mechanism design strategy was dictated by mimicking the general thematic features of DNA-binding agents[23] and cyclin-dependent kinase inhibitors[24] (Figure 1). Accordingly, we exploited the pyrimidine and fused pyrimidine scaffolds that are highly represented in lead apoptotic inducers via DNA damage[25−27] or cyclin-dependent kinase inhibition,[24,28,29] while incorporating planar rings via carbonyl and amino ligation. Hence, hydrazones of novel pyrimidinones and 1,2,4-triazolo-[4,3-*a*]pyrimidinones were rationalized as our target dual-acting molecules. The aromatic termini were then systematically substituted with various moieties influencing the steric and electronic environment thus allowing us to study the SAR among the synthesized series in quest of promising antibreast cancer agents regarding potency and selectivity. With that, the

https://doi.org/10.1021/acsomega.4c00466
ACS Omega 2024, 9, 21042−21057

Scheme 2. Synthesis of 5-Oxo-1,2,4-triazolo[4,3-*a*]pyrimidine *N*-acyl Hydrazones 17−21

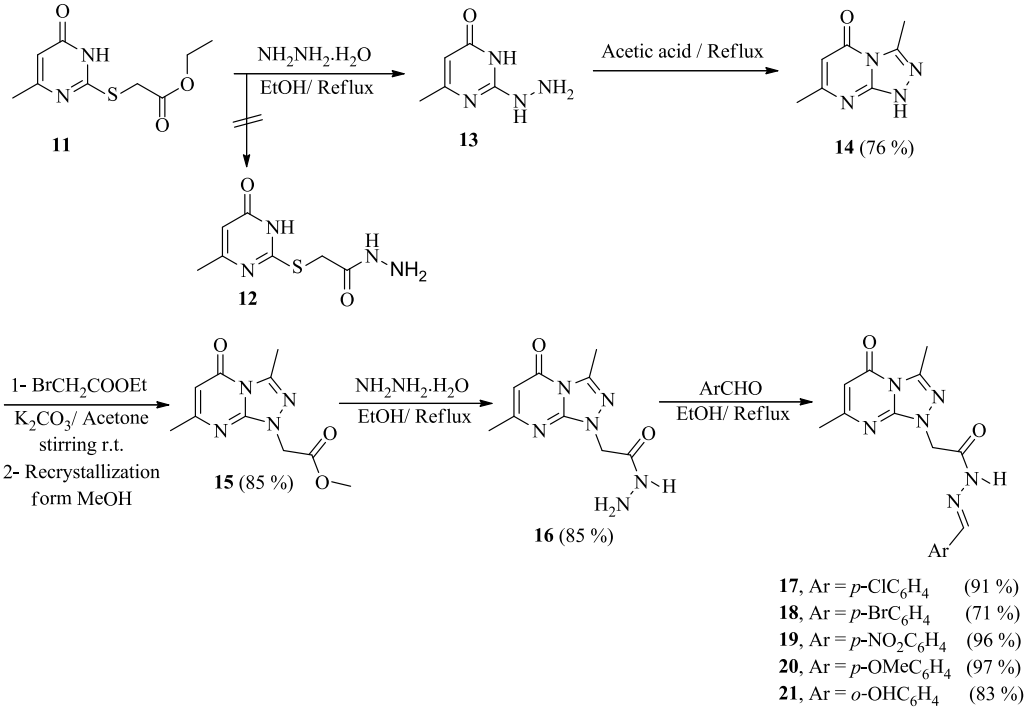

target series were screened for their potential cytotoxic activities against MCF-7 and MDA-MB237 breast cancer cells as well as Wi-38 normal human fibroblasts by MTT assay compared to the DNA intercalator doxorubicin. The most promising cytotoxic derivatives regarding potency and selectivity against breast cancer cell line over normal cells were then evaluated for their potential DNA-binding affinity utilizing luminescent terbium-(III) chloride (Tb3+) biosensor[30,31] compared to doxorubicin, followed by in vitro assessment of their CDK-2 inhibitory activities.[32,33] Breast cancer apoptosis studies were performed for cell cycle analysis and quantitation of apoptotic induction capacity of the hit compounds utilizing flow cytometry. Finally, the active derivatives−receptors binding analyses were simulated via docking and molecular dynamics to enrich the information required for concluding the structural determinants of activities.

3. RESULTS AND DISCUSSION

3.1. Chemistry. The target pyrimidinone- and triazolopyrimidinone-based S- and N-acyl hydrazones were synthesized according to the synthetic routes depicted in Schemes 1 and 2 . First, reacting 4,5-diamino-2-mercaptopyrimidin-6(1H)-one **1** with glacial acetic acid in dimethylformamide afforded the corresponding N-acetyl derivative *N*-(4-amino-2-mercapto-6-oxo-1,6-dihydropyrimidin-5-yl)acetamide **3** (Scheme 1). ^{1}H NMR spectrum of the product showed two D2O exchangeable singlet signals at δH 6.12 and 8.44 ppm corresponding to both NH_2 and N(1)H protons, respectively. NHAc and SH protons were detected downfield as an overlapped broad singlet at δH 11.79 ppm. ^{13}C NMR spectrum showed two carbonyl carbons at δC 169.9 and 173.5 ppm verifying the pyrimidinone structure of **3** and excluding the possible fused purine analogue **2**. Regioselective alkylation of **3** with ethyl bromoacetate in the presence of triethyl amine gave the *S*-alkyl derivative, ethyl 2-((5-acetamido-4-amino-6-oxo-1,6-dihydropyrimidin-2-yl)-thio)acetate **4**. The NMR spectra of **4** showed a diagnostic singlet peak resonating at δH 3.96 ppm corresponding to the SCH_2 protons correlated with its corresponding carbon assigned at δC 32.5 ppm. Compound **4** showed three carbonyl signals at δC 166.6, 169.0, and 169.5 ppm corresponding to C-6 carbonyl as well as the NHAc and the ester carbonyl groups. Treatment of **4** with hydrazine hydrate afforded the corresponding *S*-acyl hydrazide **5**. Possible amide−iminol tautomerism of the pyrimidinone ring could be detected in solution (DMSO-d_6) based on the recorded NMR spectrum, where the two tautomers were existed in nearly 1:1 ratio. This may be attributed to intramolecular interactions that could take place in polar aprotic solvent (DMSO-d_6) as reported in similar studies.[34,35] Subsequent reaction of **5** with different aldehydes under reflux gave the respective targeted *S*-acyl hydrazones **6−10** in 72−87% yield (Scheme 1).

As previously reported, acyl hydrazones can exist in two geometrical isomers (*E* and *Z*) with respect to the restricted rotation around the imine CH═N bond; however, the less hindered *E* stereoisomer is usually preferred due to its stability.[36] The existence of two conformational stereoisomers resulting from the hindered rotation around the CO−NH bond can also take place in the presence of DMSO-d_6 during performing the NMR spectral analysis. These isomers are the antiperiplanar (**ap**) and synperiplanar (**sp**), where their structure representations depend on the *anti* or *syn* disposition between the carbonyl oxygen and the proton on the neighboring nitrogen.[36,37] Several studies utilized NMR spectroscopy as a useful tool to characterize and distinguish the *N*-acyl hydrazone conformational isomers, **ap** and **sp**.[36,37] It is worth mentioning that their ratio of existence may differ according to electronic and steric factors, nature of solvent, and temperature.[38] Despite the tendency of NHC(O) bond to rapidly exchange in solution, the proton herein exhibited conspicuous NMR signals corresponding to the possible conformers allowing good assessment of data and clear structural elucidation of the synthesized hydrazones (Section 5).

https://doi.org/10.1021/acsomega.4c00466
ACS Omega 2024, 9, 21042−21057

Reacting the *S*-alkyl pyrimidinone **11** with hydrazine hydrate gave the 2-hydrazinyl-6-methyl pyrimidin-4-one **13** instead of the thiohydrazide derivative **12,** unlike the reaction of **4** with hydrazine hydrate that afforded the *S*-acyl hydrazide product **5** under similar conditions. This could be due to nucleophilic displacement of the thioalkyl group on C-2 rather than nucleophilic acyl substitution on the ester group.[34,39] Dehydrative cyclization of the hydrazinyl compound **13** using glacial acetic acid afforded 3,7-dimethyl-1,2,4-triazolo[4,3-*a*]-pyrimidin-5-one **14** (Scheme 2) which was confirmed by NMR spectra. The 1H-NMR spectrum showed a D_2O exchangeable broad singlet at δH 13.22 ppm corresponding to NH in addition to two singlet peaks at δH 2.24 and 2.70 ppm corresponding to the methyl protons of the pyrimidine and triazole moieties, respectively. Reacting a mixture of **14** with ethyl bromoacetate in slightly basic conditions afforded the corresponding ethyl ester product **15** in a good yield. It was clearly observed that transesterification reaction took place during recrystallization from methanol. X-ray crystallographic analysis of methyl 2-(3,7-dimethyl-5-oxo-1,2,4-triazolo[4,3-*a*]-pyrimidin-1(5*H*)-yl)acetate (**15**) confirmed the formation of the corresponding methyl ester and is aligned with the spectral characterization. The title compound was crystallized in the monoclinic crystal system (Figure 2). The crystal data including

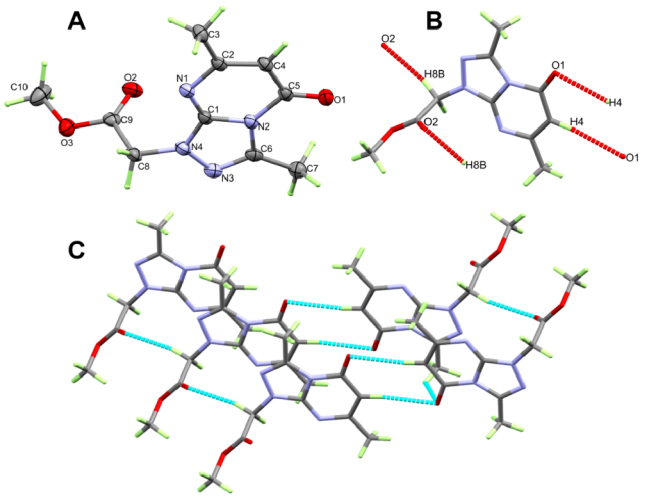

Figure 2. X-ray structure of **15** showing asymmetric unit with atom numbering (**A**), possible C−H···O interactions (**B**), and the packing scheme (**C**).

bond distances and angles are described in Table S1. The crystal structure of **15** showed no classical hydrogen bonding interactions, while the molecular packing is controlled by weak C−H···O interactions as shown in Figure 2B and listed in Table S2. View of the packing via the weak C−H···O interactions is presented in Figure 2C.

Consequent reaction of **15** with hydrazine hydrate gave the respective acyl hydrazide **16**, which was treated with different aromatic aldehydes to give the targeted *N*-acyl hydrazones **17**−**21** in 71−97% yield (Scheme 2). Referring to the previously mentioned structural arrangement across the amide CO−NH bond, the expected stereoisomers (**sp** and **ap**) of the hydrazones **17**−**21** were investigated during the performance of the NMR spectral analysis in DMSO-d_6[37] (Section 5).

3.2. Biology. *3.2.1. Cytotoxicity Screening.* The newly synthesized pyrimidine **3**−**10** and 1,2,4-triazolo[4,3-*a*]-pyrimidinone **14**−**21** derivatives were screened for their cytotoxicity against Wi-38 normal human cells in comparison with MCF-7 and MDA-MB231 breast cancer cells compared to the standard chemotherapy doxorubicin utilizing the MTT assay (Table 1).[40] Results revealed that **5**, **7**, **8**, **10**, **18,** and **21** surpassed doxorubicin. **18**, **5,** and **21** were the most promising cytotoxic agents against MCF-7 cells with IC_{50} values ranging from 0.042 to 0.052 μM and selectivity index values SI = 14.119, 16.02, and 9.961, respectively. Moderate MCF-7 cytotoxicity was observed for **10**, **7**, **8**, **19**, **9**, **4**, **14**, and **20** exhibiting IC_{50} = 0.102−0.334 μM and SI = 5.157 to 2.164. Other compounds were less active and selective against MCF-7 cells. Regarding the cytotoxicity profile against MDA-MB231 cells, the highest balanced potency and selectivity was recorded for **8** (IC_{50} = 0.583, SI = 1.222), **18** (IC_{50} = 0.559, SI = 1.060), and **9** (IC_{50} = 0.683, SI = 1.531). The remainder derivatives exhibited IC_{50} values ranging from 0.62 μM to 1.281 μM with SI < 1.2. It is worth mentioning that most of the compounds recorded higher IC_{50} and IC_{100} values against normal Wi-38 cells than doxorubicin. For all compounds, the recorded IC_{100} values were lower than the corresponding IC_{50} values against Wi-38 cells.

3.2.2. DNA Interaction Studies. Fluorescent studies were accomplished in order to study the possible DNA interaction with the studied compounds. Many fluorescent biosensors are reported in literature for assessing DNA interaction with small molecules.[41−43] Herein, terbium(III) chloride (Tb) luminescent biosensor was selected as it has superior sensitivity, selectivity over many other reported biosensors, in addition to being inexpensive with simple mix-and-read procedure.[44] Tb3+ is a trivalent lanthanide with low fluorescence in aqueous solutions.[30,31] Upon addition of the Tb biosensor to the DNA solution, it binds to DNA. The binding sites of Tb in single- and double-stranded DNA are different. In undamaged double-stranded DNA, the Tb ions are electrostatically attracted to the negatively charged phosphate backbone of the DNA. While in single-stranded DNA, it coordinates with the lone pairs of electrons of the free nucleobases. Thus, after DNA excitation, energy is transferred to the Tb biosensor causing significant elevation of its fluorescence. Thus, if the studied drug causes damage to the double-stranded DNA, there will be regions of single-stranded DNA opposite to the damaged site. Then, the Tb biosensor directly coordinates to the unpaired nucleobases of the damaged single-stranded DNA. Upon excitation at 270 nm, energy transfer to Tb occurs with significant increase in fluorescence, that is proportional to DNA damage.

For further investigation of the DNA interaction with the studied compounds, calf thymus DNA (ctDNA) was incubated with each compound for 24 h and Tb was added to each mixture. Tb fluorescence intensity was measured at 545 nm after excitation at 270 nm and was compared to all possible controls, including compound−Tb mixture, ctDNA−Tb mixture and Tb. Figure 3 presents the results obtained. As shown in Figure 3, a significant increase of Tb fluorescence appears with ctDNA samples incubated with both compounds, while minimum or no enhancement resulted from all other controls. The increase in Tb fluorescence is related to the coordination of Tb with free nucleobases at the damage sites in ctDNA that are induced by the two studied compounds. This conclusion is supported by the fact that no such change in fluorescence was observed with ctDNA and Tb controls that have no compounds added.

The potency of DNA damage induction for each of the studied compounds was assessed on natural ctDNA. Several

https://doi.org/10.1021/acsomega.4c00466
ACS Omega 2024, 9, 21042−21057

Table 1. Cytotoxicity of 3−10 and 14−21 against Wi-38, MDA-MB 231, and MCF-7 Cells and Their Selectivity Indices Utilizing MTT Assay[a]

	Wi-38		MDA-MB 231		MCF-7	
compound No.	IC_{100} (μM)	IC_{50} (μM)	IC_{50} (μM)	SI	IC_{50} (μM)	SI
3	0.103 ± 0.045	1.344 ± 0.072	1.444 ± 0.255	0.930	0.832 ± 0.048	1.615
4	0.352 ± 0.012	0.852 ± 0.011	0.840 ± 0.050	1.014	0.266 ± 0.015	3.203
5	0.240 ± 0.003	0.801 ± 0.031	0.826 ± 0.046	0.969	0.050 ± 0.008	16.02
6	0.037 ± 0.007	0.692 ± 0.064	0.681 ± 0.029	1.016	0.445 ± 0.015	1.555
7	0.232 ± 0.003	0.408 ± 0.081	0.616 ± 0.020	0.662	0.167 ± 0.040	2.443
8	0.491 ± 0.084	0.713 ± 0.044	0.583 ± 0.020	1.222	0.146 ± 0.011	4.883
9	0.424 ± 0.020	1.046 ± 0.025	0.683 ± 0.001	1.531	0.217 ± 0.016	4.820
10	0.241 ± 0.037	0.501 ± 0.049	0.590 ± 0.049	0.849	0.102 ± 0.001	4.911
14	0.206 ± 0.014	1.506 ± 0.041	1.255 ± 0.052	1.200	0.292 ± 0.010	5.157
15	0.237 ± 0.017	1.169 ± 0.022	1.281 ± 0.056	0.912	0.617 ± 0.029	1.894
16	0.115 ± 0.033	0.978 ± 0.013	1.128 ± 0.002	0.867	0.544 ± 0.008	1.797
17	0.124 ± 0.034	0.593 ± 0.024	0.632 ± 0.029	0.938	0.403 ± 0.062	1.471
18	0.111 ± 0.005	0.593 ± 0.005	0.559 ± 0.029	1.060	0.042 ± 0.009	14.119
19	0.329 ± 0.031	0.612 ± 0.034	0.820 ± 0.090	0.746	0.201 ± 0.039	3.044
20	0.280 ± 0.037	0.723 ± 0.020	0.856 ± 0.019	0.844	0.334 ± 0.020	2.164
21	0.269 ± 0.026	0.518 ± 0.008	0.697 ± 0.024	0.743	0.052 ± 0.010	9.961
DOX.	0.119 ± 0.005	0.322 ± 0.025	0.487 ± 0.018	0.661	0.198 ± 0.011	1.626

[a]All values are demonstrated as mean ± SEM.

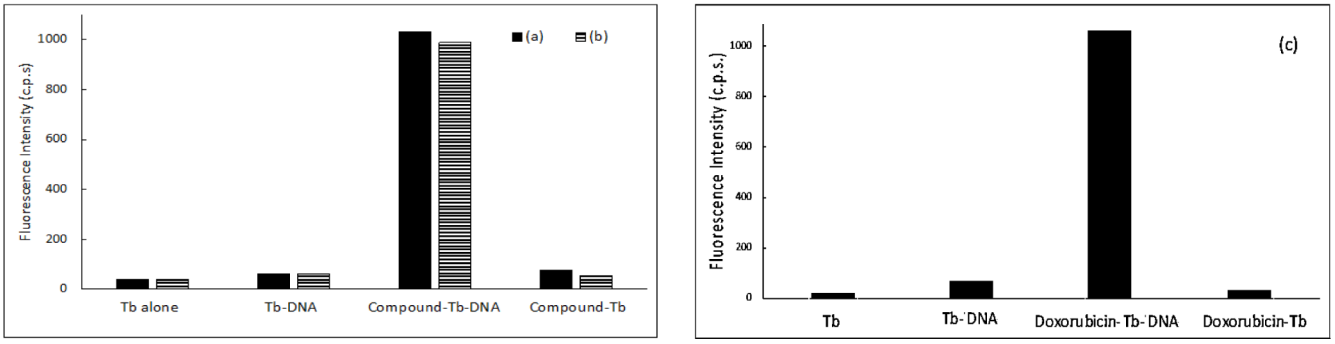

Figure 3. Tb^{3+} fluorescence enhancement at 545 nm after excitation at 270 nm of (a) **5**−DNA−Tb mixture, (b) **8**−DNA−Tb mixture, and (c) doxorubicin−DNA−Tb^{3+} mixture. Controls such as DNA−Tb mixture, **5**−Tb mixture, **8**−Tb mixture, doxorubicin−Tb^{3+} mixture, and Tb alone are also presented.

concentrations within the range of 0.1 pM−10.0 μM of each of the studied compounds were incubated with ctDNA for 24 h. After which, Tb solution was added to aliquots of such mixtures and the fluorescence intensity was recorded. Figure 4 presents the fluorescence intensity as a function of the compound concentration for various compound/ctDNA/Tb mixtures. At zero concentration of the studied compound, minimum Tb fluorescence was recorded. This reflects that the DNA molecule is undamaged, intact, and forming a double helix. In this conformation, Tb ions are electrostatically attracted to the negatively charged DNA-phosphate backbone showing no increase in its fluorescence. For solutions with higher concentrations of the studied compound, Tb fluorescence increased proportionally with the concentration until a concentration of 1, 3, and 4 μM for **5**, **8**, and doxorubicin, respectively, where no further increase in the fluorescence occurs. This reflects that more DNA damage is induced with increasing concentrations of the two studied compounds. At concentrations higher than 1 and 3 μM for **5** and **8**, respectively, Tb fluorescence remains constant at high fluorescence levels. This indicates that maximum DNA damage has occurred. Table 2 shows the analytical parameters elucidated from Figure 4 for quantifying any DNA damage induced by the two studied compounds. The linearity parameters were calculated from the calibration curve in Figure 4 inset to obtain the minimum concentration of the studied compounds that would induce DNA damage. Results show that a concentration as low as 10.64, 30.03, and 0.76 nM of **5**, **8**, and doxorubicin, respectively, is enough to induce detectable damage in ctDNA (Table 2) indicating their potency to induce DNA damage in natural DNA. It is obvious that doxorubicin is the most potent compound; however, very small concentrations of both **5** and **8** are still enough to cause detected DNA damage.

3.2.3. CDK-2 Inhibition. In vitro CDK-2 inhibition profiles of the derivatives under investigation **5** and **8** were studied in reference to the standard sorafenib. Both compounds exhibited in vitro enzymatic inhibition within their cytotoxic IC_{50} ranges especially against MDA-MB 231 cells. Herein, **5** (IC_{50} = 0.172 μM) was slightly more potent than **8** (IC_{50} = 0.189 μM) (Table 3). However, both were less active than the reference sorafenib (IC_{50} = 0.029 μM).

3.3. Docking and Molecular Dynamics Simulations. *3.3.1. DNA Binding Mode Analysis.* The studied pyrimidine derivatives **5** and **8** were docked into the prepared DNA dodecamer (PDB code: 2DND[45] employing Molecular Orbital Environment MOE 2019.102[46] to simulate their possible DNA-

https://doi.org/10.1021/acsomega.4c00466
ACS Omega 2024, 9, 21042−21057

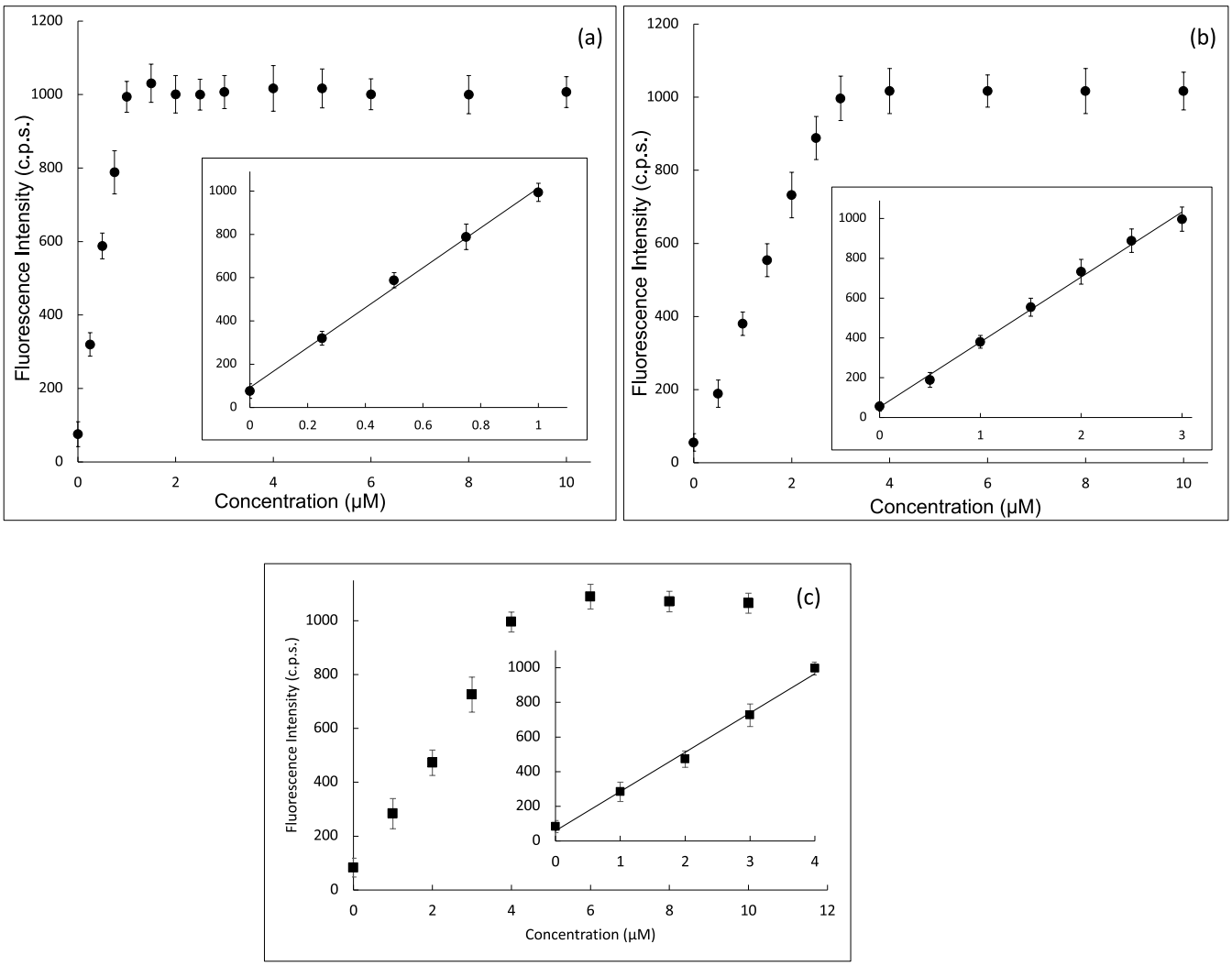

Figure 4. Effect of increasing concentration of (a) **5**, (b) **8**, and (c) doxorubicin on the fluorescence of Tb−ctDNA complex. The insets show the fit to the linear region of the constructed plots.

Table 2. Analytical Parameters for the Fluorescence Measurements of the Studied Compounds with ctDNA Mixtures

parameter	5-ctDNA	8-ctDNA	doxorubicin + ctDNA
linear dynamic range	0.1 pM−1.0 μM	0.1 pM−3.0 μM	0.00 μM−4.00 μM
correlation coefficient (r)	0.997	0.996	0.994
intercept[a]	92.09	52.22	22.67
slope[b]	922.15	326.78	5878
LOD[a] (nM)	10.64	30.03	0.76
LOQ[a] (nM)	35.48	100.12	2.56

[a]LOD: Limit of detection. [b]LOQ: Limit of quantitation.

binding modes compared to the cocrystallized ligand distamycin. The most stable conformers were explored for their possible 2D and 3D interactions (Figure 5).

Both the studied compounds **5** and **8** fitted between the DNA double strand within the cocrystallized ligand binding site of the prepared dodecamer recording free energy of binding (ΔG) of −6.42 and −8.53 kcal/mol, respectively compared to distamycin (ΔG = −11.29 kcal/mol). As illustrated (Figure 5A,B), *N*-(4-Amino-2-((2-hydrazinyl-2-oxoethyl)thio)-6-oxo-1,6-dihydropyrimidin-5-yl)acetamide **5** is bonded with the DNA strands via four key H-bond interactions linking the thymidine bases of DT:A7, DT:A8, and DT:B20 to the hydrazide side chain, the pyrimidine core, and the amino group, respectively. On the other hand, (*E*)-*N*-(4-amino-2-((2-(2-(4-nitrobenzylidene)-hydrazinyl)-2-oxoethyl)thio)-6-oxo-1,6-dihydropyrimidin-5-yl)acetamide **8** interacted with the thymidine of DT:A6 and the guanine DG:B22 via H-bond interactions through the hydrazone. The compound's backbone was oriented between the DNA strands so that both the triazole and the triazine rings were posed toward thymidine base of DT:B21 displaying two π−H bond interactions.

3.3.2. CDK-2 Binding Mode Analysis and Molecular Dynamics Simulations. Docking of **5** and **8** was simulated into the prepared CDK-2 active domain (PDB code: 2FVD)[47]

https://doi.org/10.1021/acsomega.4c00466
ACS Omega 2024, 9, 21042−21057

Table 3. Inhibitory Profiles of 5 and 8 against CDK-2

Compound No.	Structure	IC_{50} (μM)
5	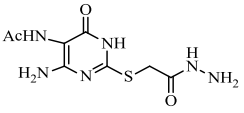	0.172 ± 0.00498
8	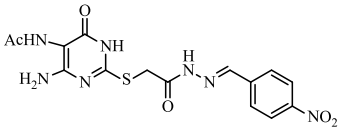	0.189 ± 0.00513
Sorafenib	-----	0.29 ± 0.00107

Table 4. Hydrogen Bonding Interaction Details and Their Occupancies

donor	acceptor	occupancy
LEU83-main-N	LIG585-side-O1	85.83%
LIG585-side-N2	GLU81-main-O	79.94%
LIG 585-Sside-N5	ASP145-Sside-OD2	36.53%
LIG585-side-N3	LEU83-main-O	28.94%
LYS33-side-NZ	LIG585-side-N6	15.37%
LYS33-side-NZ	LIG585-side-N5	7.98%
LIG585-side-N5	ASP145-side-OD1	49.90%

employing MOE 2019.102[46] compared to the cocrystallized pyrimidine-based inhibitor (Figure 6).

Both **5** and **8** resided in the ligand-binding site with free energy of binding (ΔG) of −6.24 and −7.50 kcal/mol, respectively, compared to the redocked reference (ΔG = −9.16 kcal/mol). Figure 6A,B showed that *N*-(4-amino-2-((2-hydrazinyl-2-oxoethyl)thio)-6-oxo-1,6-dihydropyrimidin-5-yl)-acetamide **5** interacted with the key amino acid residues Phe82 and Leu 83 via two H-bonds linking the core carbonyl oxygen with the enzymatic active site resembling the cocrystallized ligand interactions. (*E*)-*N*-(4-amino-2-((2-(2-(4-nitrobenzylidene)hydrazinyl)-2-oxoethyl)thio)-6-oxo-1,6-dihydropyrimidin-5-yl)acetamide **8** also posed H-bond interaction between the core carbonyl group and the active site Leu83 in addition to a H-bond interaction with Asp145 and π−H bond with Phe80 through the hydrazone side chain.

Compound **8** was selected for molecular dynamics studies, as it recorded more favorable binding affinity (ΔG), interactions and receptor occupancy (Figure 6) compared to compound **5**. The best docking pose for compound **8** in complex with the prepared protein 2FVD was further evaluated for its binding stability employing molecular dynamics simulations run for 100 ns at natural room temperature along with its apoprotein form for comparison. Visualization of the trajectories post simulations revealed that compound **8** remained bound to the active site pocket. Root-mean-square deviation (RMSD), root-mean-square fluctuation (RMSF), radius of gyration (RoG), hydrogen bonding, average center of mass (COM), distance between 2FVD and the docked compound **8**, secondary structure analysis (DSSP), and binding free energy (MMPBSA) were computed. Figure 7A shows the RMSD for the 2FVD-**8** complex structure and apoprotein during 100 ns simulations. While 2FVD-**8** complex, 2FVD backbone in 2FVD-8 simulation, and free 2FVD RMSD curves showed stability after 10 ns of simulation time, free 2FVD RMSD experienced more fluctuations with simulation time. This observation highlighted the increased stabilization of 2FVD when complexed with the studied compound **8**. The ligand-**8** RMSD curve in the complex simulation was fairly steady reflecting the ligand's stability in the binding site. The RoG analysis (Figure 7C) was also consistent with RMSD results for the complex, being stable with negligible fluctuations (≤0.5 Å) throughout the whole simulation compared with the free 2FVD form indicating the compactness and the stability of the protein−ligand system. RMSF was calculated for the protein complex based on "*C*-alpha" atoms using GROMACS program. Overall, the fluctuation intensity remains below 2.0 Å for the compound except for some residues which represent a loop or turn in the protein (Figure 7B). Both the free 2FVD and 2FVD-**8** complex showed similar drift for most amino acid residues except for multiple amino acids regions showing more stabilization in the presence of ligand **8.** Herein, ligand interactions might explain this stability. The total number of hydrogen bonds formed between the studied derivative **8** and the protein 2FVD during 100 ns of the simulation time are shown in Figure 7D. **8** maintained an average of four hydrogen bonds during the simulation time and had no significant time gaps where no hydrogen bonding was present. The average COM distance between ligand and protein during 100 ns of the simulation time is shown in Figure 8B. The 2FVD-**8** system showed very small fluctuation of COM distance within 2.5−3 Å or less, indicating that the ligand resided well in its binding site. To further evaluate the binding between the 2FVD and the ligand **8**, detailed hydrogen bonding formation and contact frequency (CF) analysis were both performed using a VMD script (contactFreq tcl module), where a contact is defined as the amino acid being within a distance cutoff of 4 Å. Table 4 shows the detailed hydrogen bonding interactions and their occupancies, whereas Figure 9 shows the CF analysis results. As illustrated, the shared residues with the highest CF were Val18, Lys33, Phe80, Glu81, Leu83, Leu134, and Asp145. Figure 10 shows snapshots of the first and last frame of the 2FVD-**8** simulation and the interaction diagram of the protein−ligand at the last frame of the simulations. Most of the high CF protein residues are still in active interaction with the ligand **8,** which confirmed its stability even at the last moment of the simulation. The DSSP algorithm was used to investigate changes in the secondary structure during the course of the simulations. Three areas were evaluated for structural alterations following ligand **8** complexation in comparison to the free 2FVD (Figure 11). Structural differences in residues 285−293, 221−245, 125−133, and most importantly residues 31−61 were clear as illustrated in Figure 11. Finally, the MM/PBSA method was selected for rescoring complex being the fastest force field-based method that can compute the free energy of binding, as compared to the other computational free energy methods such as free energy perturbation and thermodynamic integration methods. The MM/PBSA calculation was performed using g-mmpbsa software, and the calculated binding free energies are shown in Table 5.

3.4. Apoptosis Studies. *3.4.1. MCF-7 Cell Cycle Arrest.* MCF-7 cell cycle analysis and quantification of apoptosis induction were performed following 24 h treatment with IC_{50} of the hit compound **5** (Figure 12). Results revealed interference with the cell cycle distribution with reduced content during G1 and G2/M phases and increased DNA content during S compared to the cell cycle of untreated cells. These observations are mirrored by DNA degradation, CDK-2 inhibition,[32,33] and apoptosis induction.

3.4.2. Analysis of MCF-7 Cell Apoptosis Induction. The apoptotic induction potential of compound **5** in MCF-7 cells

https://doi.org/10.1021/acsomega.4c00466
ACS Omega 2024, 9, 21042−21057

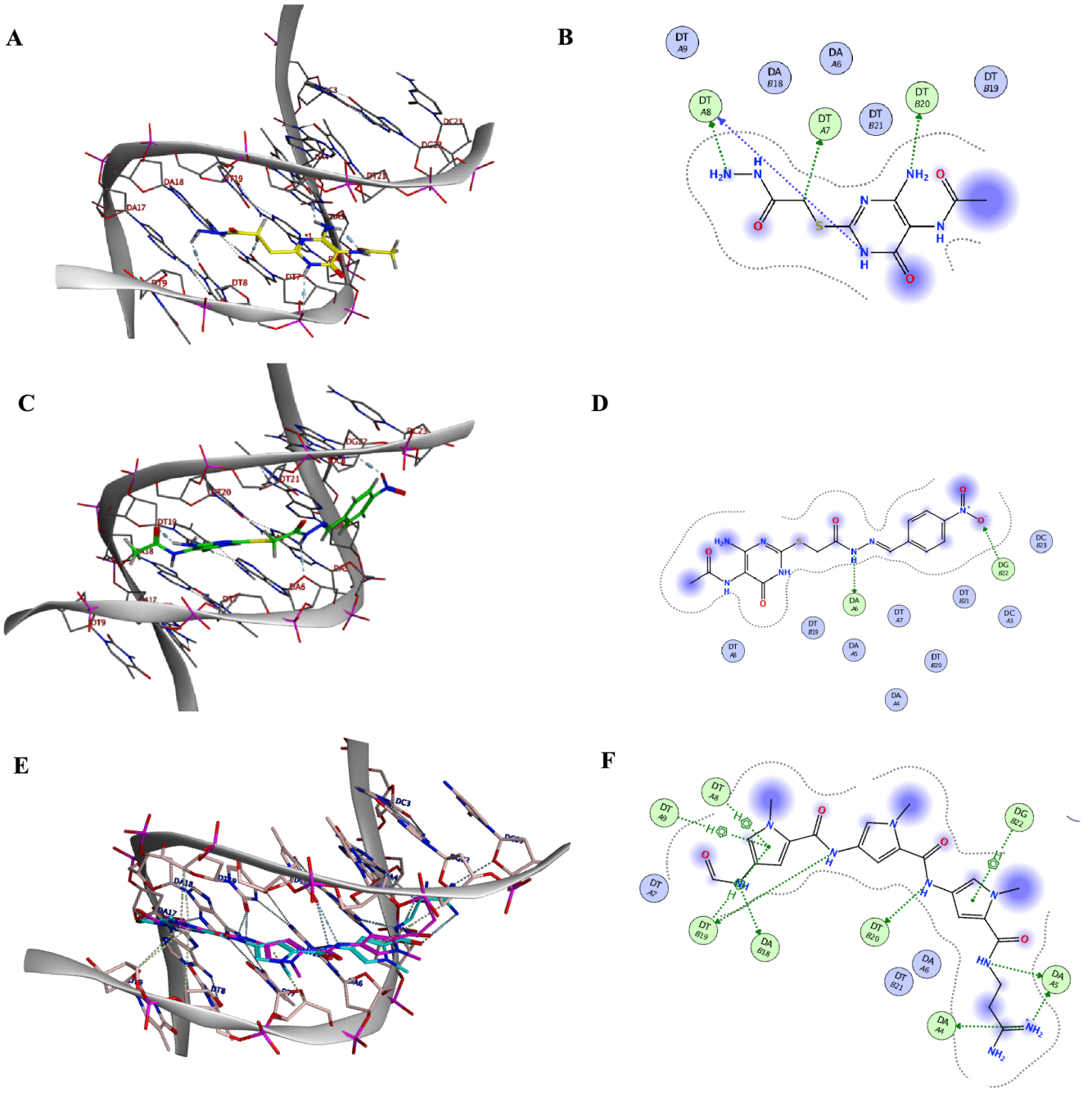

Figure 5. (A) 3D binding mode of **5** (yellow sticks), (B) 2D interactions of **5**, (C) 3D binding mode of **8** (green sticks), (D) 2D interactions of **8**, (E) overlay of the docked (cyan sticks) and cocrystallized ligand, distamycin (violet sticks), and (F) 2D interaction of distamycin with DNA bases of DNA dodecamer (gray ribbon) (PDB code: 2DND). For 2D interactions, hydrogen bond interactions are illustrated as green dotted arrows and π−H or π−π interactions are presented in green dotted lines.

was quantified by the annexin V and propidium iodide double staining assay displaying the biparametric cytofluorimetric analysis of apoptotic, necrotic, and viable populations (Figure 13). A 24 h treatment of MCF-7 cells with IC_{50} of **5** induced total cell death by 46.75% with pronounced early apoptosis (29.11%) relative to the late stage (17.64%) compared to control MCF-7 cells (0.73%). The study showed a mild increase in the recorded necrotic cells (5.39%) relative to the control (1.34%).

3.5. Structure−Activity Relationship. The MTT assay results revealed that the studied pyrimidine **3−10** and 1,2,4-triazolo[4,3-*a*]pyrimidinone **14−21** scaffolds (Figure 1) generally exhibited promising cytotoxicity profiles against MCF-7 and MDA-MB231 cells. However, their potency and selectivity to the tested breast cancer cell lines over normal human cells were functions of the nature of the heterocyclic core and the terminal phenyl substituents. Within the *N*-(4-amino-2-(substituted benzylidene)hydrazinyl)-2-oxoethyl)thio)-6-oxo-1,6-dihydropyrimidin-5-yl)acetamides **6−10**, the terminal phenyl substitution affected the observed cytotoxic activity against MCF-7 to lesser extent. The derivatives substituted with bromo (**7**), nitro (**8**), and hydroxy (**10**) groups were nearly equipotent, whereas the methoxy (**9**) and the chloro (**6**) derivatives were less active, respectively. Similarly, the series

https://doi.org/10.1021/acsomega.4c00466
ACS Omega 2024, 9, 21042−21057

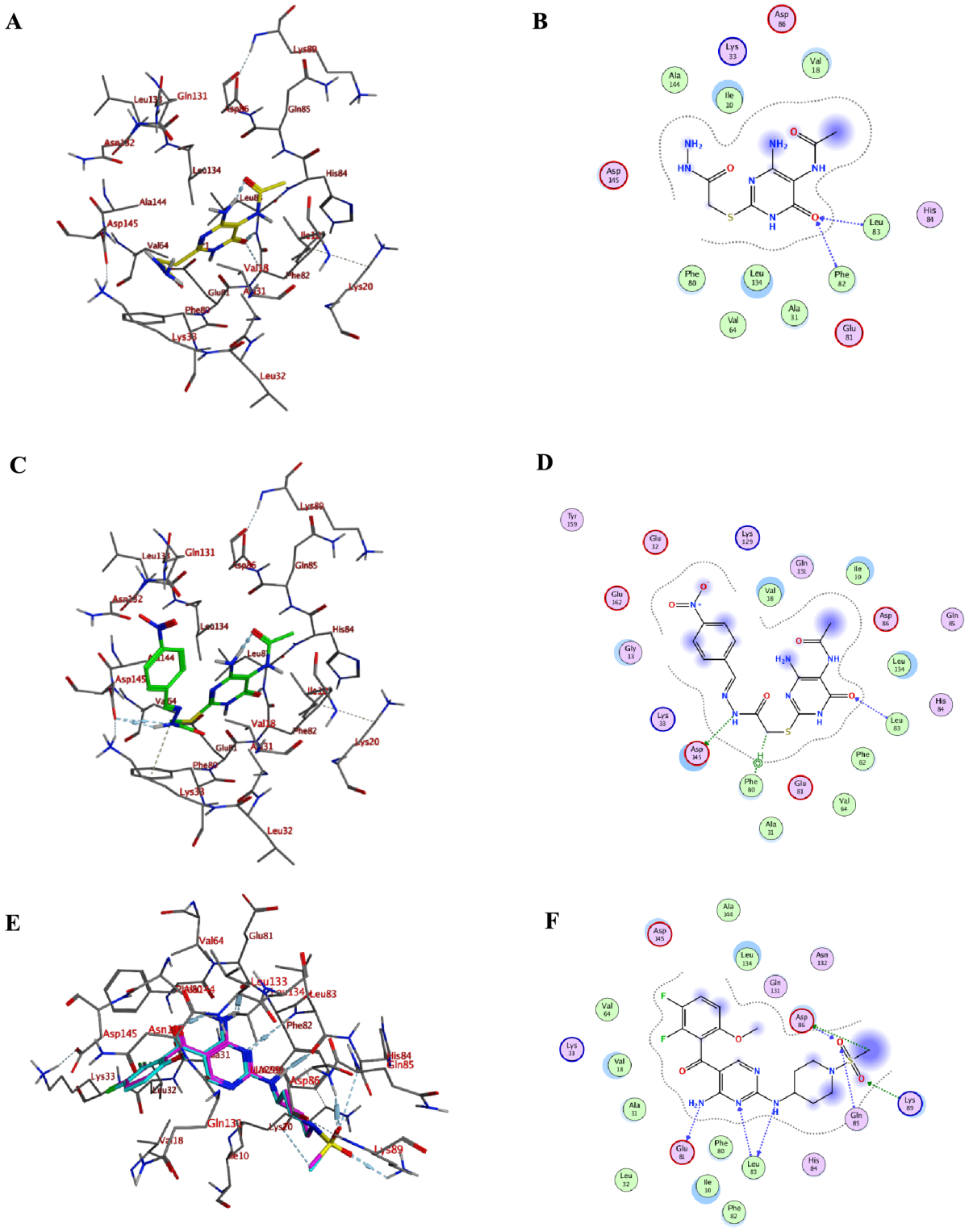

Figure 6. (A) 3D binding mode of **5** (yellow sticks), (B) 2D interactions of **5**, (C) 3D binding mode of **8** (green sticks), (D) 2D interactions of **8**, (E) overlay of the docked (cyan sticks) and cocrystallized reference CDK-2 inhibitor, (4-Amino-2-((1-(methylsulfonyl)piperidin-4-yl)amino)pyrimidin-5-yl)(2,3-difluoro-6-methoxyphenyl)methanone (violet sticks), and (F) 2D interaction of CDK-2 active domain (PDB code: 2FVD). For 2D interactions, hydrogen bond interactions are illustrated as green dotted arrows and $\pi-H$ or $\pi-\pi$ interactions are presented in green dotted lines.

exhibited comparable activities against MDA-MB231. However, the nitro derivative **8** exhibited the most balanced cytotoxic profile against MDA-MB231 cells in terms of potency and selectivity. Obviously, the hydrazide precursor **5** recorded the most potent activity against MCF-7 with outstanding selectivity compared to all the studied compounds.

Among the evaluated 5-oxo-1,2,4-triazolo[4,3-*a*]-pyrimidinone *N*-acyl hydrazones **17**−**21**, the terminal bromo (**18**) and hydroxy (**21**) substituents conferred the highest

https://doi.org/10.1021/acsomega.4c00466
ACS Omega 2024, 9, 21042−21057

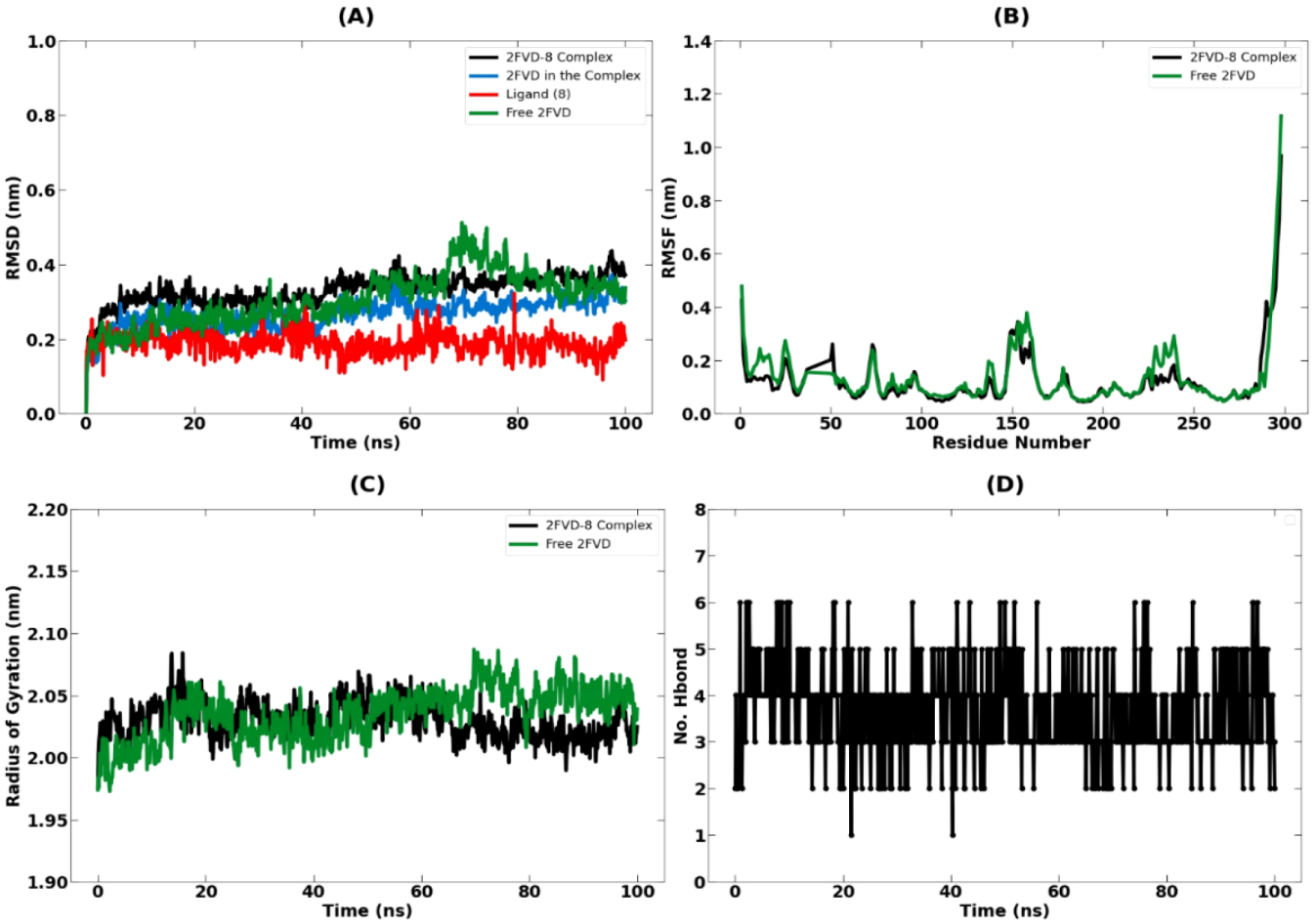

Figure 7. (A) Complex RMSD, (B) RMSF, (C) radius of gyration, and (D) hydrogen bonding of 2FVD in and without the presence of the ligand 8 during 100 ns MD simulation.

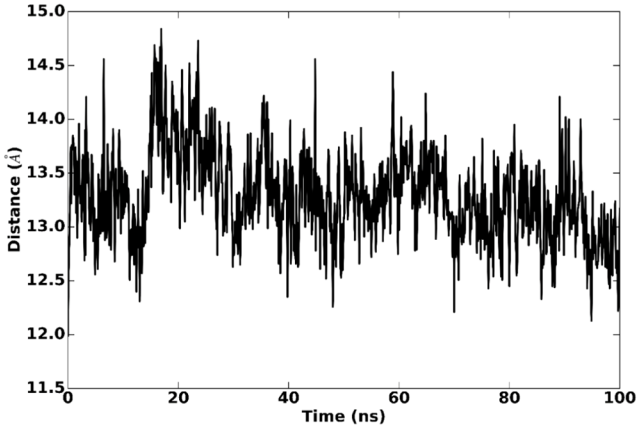

Figure 8. Average distance between the ligand **8** and the protein of the 2FVD-8 complex during 100 ns MD simulation.

detected potency and selectivity to the scaffold against MCF-7 cells. Substitution of the terminal bromo (**18**) by chloro (**17**) or nitro group (**19**) reduced the compounds' potency and selectivity by 5- or 10-folds, respectively. Similarly, methylation of the hydroxyl group (**21**) led to more than 6-fold reduction in the observed MCF-7 cytotoxicity. On the other hand, the cytotoxic profile of the studied series against MDA-MB231 cells followed different trend, where the evaluated hydrazones **17**−**21** showed comparable potency and selectivity.

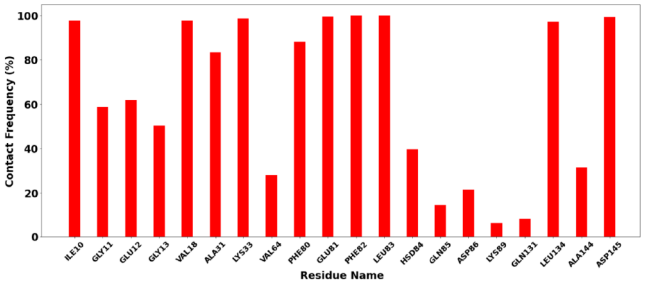

Figure 9. Contact frequency analysis of the complexes.

4. CONCLUSION

This study portrays the design, synthesis, and evaluation of novel pyrimidine **3**−**10** and 1,2,4-triazolo[4,3-*a*]pyrimidinone **14**−**21** derivatives as dual DNA-damaging agents and CDK-2 inhibitors for synergistic apoptotic induction of breast cancer cells. The design relied on representing the main thematic pharmacophoric requirements of lead compounds. Initial cytotoxicity screening of the synthesized derivatives was performed against MCF-7 and MDA-MB231 breast cancer cells and normal fibroblasts Wi-38 in reference to doxorubicin. *N*-(4-amino-2-((2-hydrazinyl-2-oxoethyl)thio)-6-oxo-1,6-dihydropyrimidin-5-yl)acetamide **5** and its *p*-nitro substituted hydrazone derivative **8** were the hit compounds regarding safety and potency against MCF-7 (IC_{50} = 0.050 μM and 0.146 μM, SI =

https://doi.org/10.1021/acsomega.4c00466
ACS Omega 2024, 9, 21042−21057

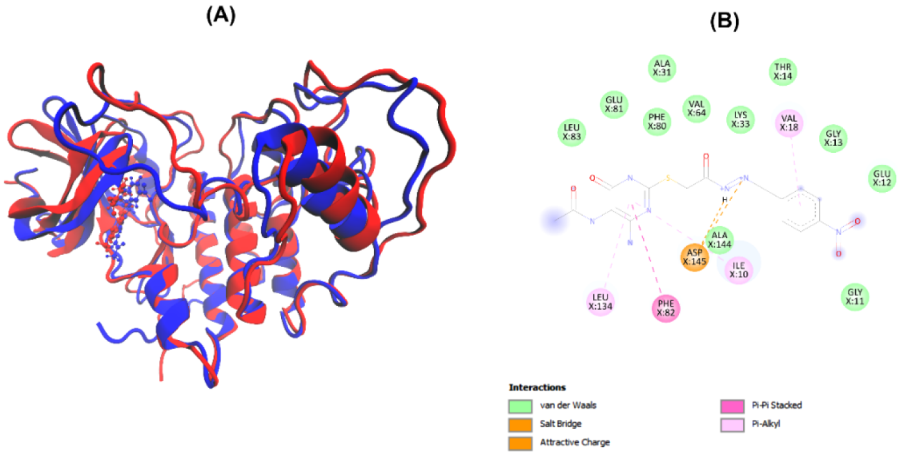

Figure 10. (A) 2FVD-**8** Protein−ligand complex in the first (blue structure) and last frame (red structure) of the simulation and (B) 2D interaction diagram at the last snapshot of 100 ns simulation.

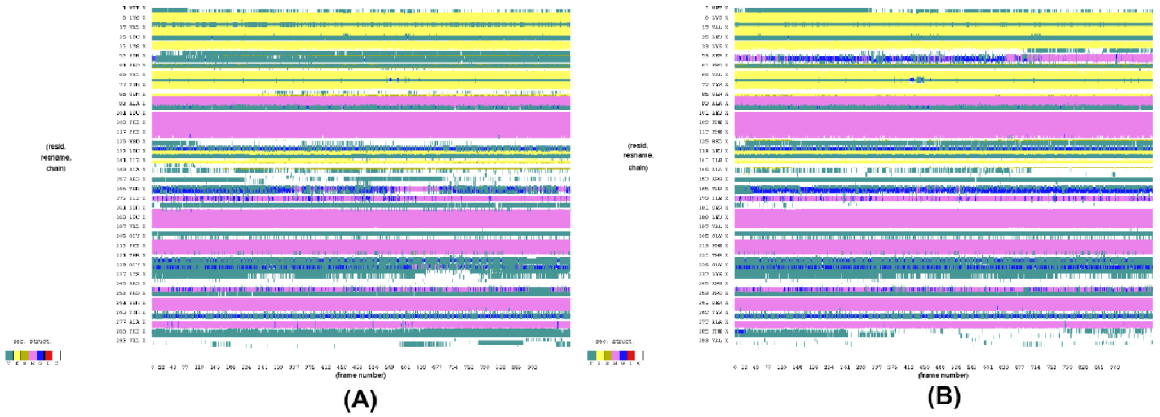

Figure 11. Dynamic evolution of the secondary structure fluctuations (DSSP analysis) of (A) free 2FVD and (B) 2FVD-**8** complex structures.

Table 5. Calculated Binding Free Energies of Tested Compound 8 in Complex with 2FVD [kJ/mol]

complex	ΔG	van der Waals energy	electrostatic energy	polar solvation energy	SASA energy
2FVD-8	−119.930 ± 34.278	−155.828 ± 22.010	−179.544 ± 67.241	233.601 ± 29.900	−18.159 ± 1.951

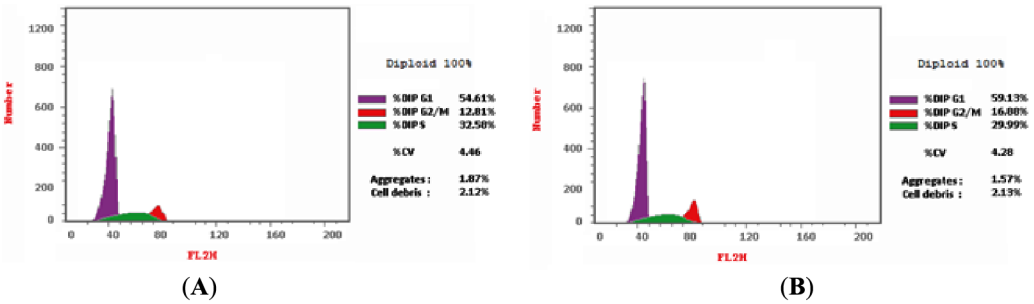

Figure 12. (A) MCF-7 cell cycle analysis following 24 h treatment with (A) in comparison to (B) control untreated cells. Color index of the cell cycle phases illustrated as violet for the G1, red for red for the G2/M and green for the S phase.

16.02 and 4.883, respectively) and MDA-MB231 (IC_{50} = 0.826 μM and 0.583 μM, SI = 0.969 and 1.222, respectively). Mechanistic studies revealed that both derivatives could bind to DNA and induce its damage at nanomlar concentrations (10.64 and 30.03 nM, respectively) together with CDK-2 inhibition at submicromolar IC_{50} (0.172 and 0.189 μM, respectively). Accordingly, **5** disrupted the MCF-7 cell cycle distribution in the S phase and induced cells apoptosis by 46.75%. Docking simulations declared their possible receptors binding modes and aided concluding the significance of the adopted design rationale. MD simulations highlighted the stability of the docked complex. With that, the hit compounds could be exploited for further optimization studies in quest for more potent dual acting apoptotic inducers for combating breast cancer cells.

https://doi.org/10.1021/acsomega.4c00466
ACS Omega 2024, 9, 21042−21057

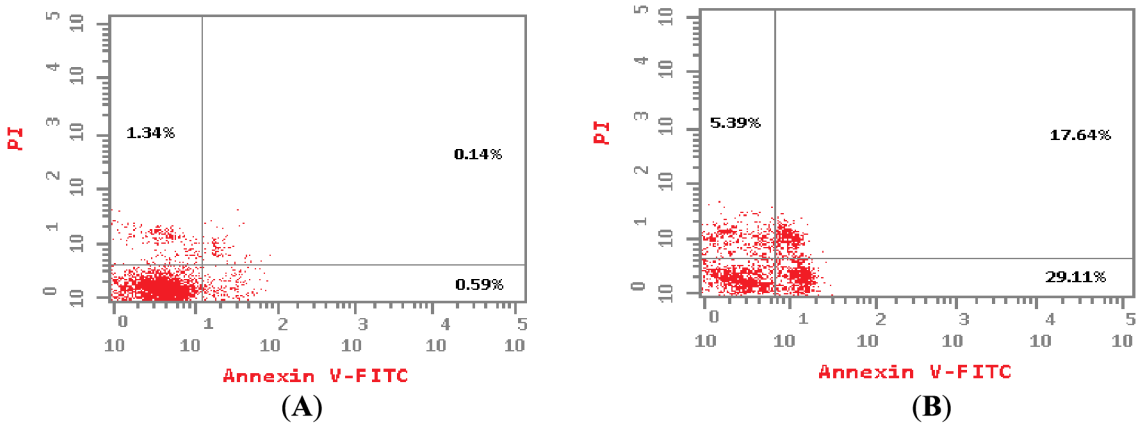

Figure 13. Apoptosis induction analysis by flow cytometry in MCF-7 cells after 24 h treatment with (A) dot plot chart of untreated MCF-7 cells, (B) dot plot chart of compound 5-treated MCF-7 cells, and quantifying cell populations in quadrants; late apoptosis (upper right), early apoptosis (lower right), necrosis (upper left), and viable cells (lower left).

5. EXPERIMENTAL SECTION

5.1. Chemistry. *5.1.1. Materials and Methods.* All the techniques, instruments and methods used are detailed and mentioned in the Supporting Information.

*5.1.2. Synthesis of N-(4-amino-2-substituted-6-oxo-1,6-dihydropyrimidin-5-Yl)acetamide (**3**−**10**). 5.1.2.1. N-(4-amino-2-mercapto-6-oxo-1,6-dihydropyrimidin-5-yl)-acetamide (**3**).* Refluxing 4,5-diamino-2-mercaptopyrimidin-6(3*H*)-one **1** (1 g, 6 mmol) and glacial acetic acid (20 mL) in DMF (0.5 mL) for 3 h gave **3** as a yellow precipitate which was filtered then recrystallized from ethanol in 87% yield; mp decomp. > 280 °C, R_F = 0.23 (CH_2Cl_2/ CH_3OH 4:1). ^{1}H NMR (500 MHz, DMSO-d_6) δ ppm: 1.62, 1.87 (2 s, 3 H, CH_3CO **A, B**), 6.12, 6.43 (2 s, 2 H, D_2O exchangeable NH_2 **A, B**), 8.44 (s, 1 H, D_2O exchangeable N(1)H + OH), 11.79 (bs, 2 H, D_2O exchangeable NH, SH). ^{13}C NMR (125 MHz, DMSO-d_6) δ ppm: 23.2 ($\underline{C}H_3CO$), 92.0 (C-5), 151.3 (C-4), 159.8 (C-2), 169.9 (C-6), 173.5 ($CH_3\underline{C}O$).

*5.1.2.2. Ethyl 2-((5-Acetamido-4-amino-6-Oxo-1,6-dihydropyrimidin-2-yl)thio)acetate (**4**).* A mixture of **3** (0.6 g, 3.3 mmol) and triethylamine (0.6 mL, 4.3 mmol) in acetone (140 mL) was stirred for 15 min, then ethyl bromoacetate (0.4 mL, 3.6 mmol) was added to the reaction mixture. The stirring was continued for another 48 h at room temperature. The white precipitate obtained was filtered off, washed with water and dried. The crude product was recrystallized from absolute ethanol to give white crystals of **4** in 80% yield; mp 215−218 °C, R_F = 0.46 (CH_2Cl_2/ CH_3OH 4:1). ^{1}H NMR (500 MHz, DMSO-d_6) δ ppm: 1.16 (t, 3 H, J = 7.0 Hz, $\underline{CH_3}CH_2$), 1.61, 1.87 (2 s, 3 H, CH_3CO **A, B**), 3.96, 3.97 (2 s, 2 H, $\underline{SCH_2}$ **A, B**), 4.09 (q, 2 H, J = 14 Hz, $\underline{CH_2}CH_3$), 6.17, 6.49 (2 s, 2 H, D_2O exchangeable NH_2 **A, B**), 8.50 (s, 1 H, D_2O exchangeable N(1)H + OH), 11.98 (bs, 1 H, D_2O exchangeable NH). ^{13}C NMR (125 MHz, DMSO-d_6) δ ppm: 14.5 ($\underline{C}H_3CH_2$), 20.5, 23.3 ($\underline{C}H_3CO$ **A, B**), 31.2, 32.5 (SCH_2 **A, B**), 61.7 (OCH_2), 95.2 (C-5), 159.2 (C-4), 161.0 (C-2), 166.6 (C-6), 169.0, 169.5 (2 CO). Anal. Calc. for $C_{10}H_{14}N_4O_4S$: C, 41.95; H, 4.93; N, 19.57; S, 11.20. Found: C, 42.07; H, 4.75; N, 19.78; S, 11.08.

*5.1.2.3. N-(4-amino-2-((2-hydrazinyl-2-oxoethyl)thio)-6-oxo-1,6-dihydropyrimidin-5-yl)acetamide (**5**), amide (**A**)-iminol (**B**) tautomers.* A solution of **4** (0.11 g, 0.41 mmol) in ethanol (40 mL) and hydrazine hydrate (0.08 mL, 1.6 mmol) were refluxed for 6 h. The white precipitate formed was filtered off, washed with ethanol, and dried then recrystallized from ethanol/H_2O as a white powder in 65% yield; mp decomp. 248 °C, R_F = 0.47 (CH_2Cl_2/ CH_3OH 3:2). ^{1}H NMR (500 MHz, DMSO-d_6) δ ppm: 1.61, 1.85, 1.88 (3 s, 3 H, CH_3 **A, B**), 3.61, 3.65 (2 s, 2 H, SCH_2 **A, B**), 5.77, 6.06 (2 bs, 2 H, D_2O exchangeable NH_2 **A, B**), 6.27 (bs, 1 H, D_2O exchangeable NH), 8.22, (s, 0.5 H, D_2O exchangeable N(1)H **A**), 8.53 (s, 0.5 H, D_2O exchangeable OH **B**), 9.12 (bs 1H, D_2O exchangeable NH). ^{13}C NMR (125 MHz, DMSO-d_6) δ ppm: 23.32, 23.35 (CH_3 **A, B**), 32.3 (SCH_2), 90.0, 95.1 (C-5 **A, B**), 155.3 (C-6 **B**), 159.2, 159.7 (C-4 **A, B**), 161.0, 161.3 (C-2 **A, B**), 167.4 (C-6 **A**), 169.5, 169.8 (2 CO). Anal. Calc. for $C_8H_{12}N_6O_3S$: C, 35.29; H, 4.44; N, 30.86; S, 11.78. Found: C, 35.46; H, 4.62; N, 30.94; S, 11.95. HRMS (ESI) m/z Calcd For $C_8H_{12}N_6O_3S$ $[M + 1]^+$: 273.0770; found 273.0777.

*5.1.3. General Procedure for the Synthesis of (E)-N-(4-amino-2-((2-(2-(substitutedbenzylidene)hydrazinyl)-2-oxoethyl)thio)-6-oxo-1,6-dihydropyrimidin-5-yl)acetamide (**6**−**10**).* Hydrazones **6**−**10** were produced by refluxing a mixture of compound **5** (1 mmol) with aryl aldehyde (1 mmol) in ethanol (40 mL) for 4−6 h in the presence of glacial acetic acid (2 drops) as a catalyst. The crude products precipitated were filtered off, dried and recrystallized from ethanol.

*5.1.3.1. (E)-N-(4-amino-2-((2-(2-(4-chlorobenzylidene)-hydrazinyl)-2-oxoethyl)thio)-6-oxo-1,6-dihydropyrimidin-5-yl)acetamide (**6**).* Yield 72%, mp 246−247 °C, R_F = 0.61 (CH_2Cl_2/ CH_3OH 4:1). ^{1}H NMR (500 MHz, DMSO-d_6) δ ppm: 1.61, 1.88 (2 s, 3 H, CH_3), 3.85 (s, 0.6 H, SCH_2 **ap**), 4.35 (s, 1.2 H, SCH_2 **sp**), 6.21 (bs, 2 H, D_2O exchangeable NH_2), 7.47 (d, 2 H, J = 8.5 Hz, Ar−H), 7.67 (t, 2 H, Ar−H), 7.95 (s, 0.6 H, CH═N **sp**), 8.17 (s, 0.33 H, CH═N **ap**), 8.52, 8.54 (2 s, 1 H, D_2O exchangeable N(1)H **sp** + **ap**), 11.54, 11.64 (2 s, 1 H, D_2O exchangeable NH **sp** + **ap**), 11.94 (bs, 0.5 H, D_2O exchangeable NHAc). ^{13}C NMR (125 MHz, DMSO-d_6) δ ppm: 23.3 (CH_3), 32.3 (SCH_2 **sp**), 33.3 (SCH_2 **ap**), 95.2 (C-5), 129.1, 129.2, 129.4, 133.5, 133.6, 134.8, 135.0 (Ar−C), 142.7 (CH═N **sp**), 146.2 (CH═N **ap**), 159.2 (C-4), 161.0 (C-2), 164.6 (C-6), 169.55, 169.59 (2 CO). Anal. Calc. for $C_{15}H_{15}ClN_6O_3S$: C, 45.63; H, 3.83; N, 21.28; S, 8.12. Found: C, 45.85; H, 3.70; N, 21.53; S, 8.30.

*5.1.3.2. (E)-N-(4-amino-2-((2-(2-(4-bromobenzylidene)-hydrazinyl)-2-oxoethyl)thio)-6-oxo-1,6-dihydropyrimidin-5-yl)acetamide (**7**).* Yield 76%, mp 254−256 °C, R_F = 0.58 (CH_2Cl_2/ CH_3OH 4:1). ^{1}H NMR (500 MHz, DMSO-d_6) δ

https://doi.org/10.1021/acsomega.4c00466
ACS Omega 2024, 9, 21042−21057

ppm: 1.61, 1.88 (2 s, 3 H, CH_3), 3.84 (s, 0.7 H, SCH_2 **ap**), 4.35 (s, 1.2 H, SCH_2 **sp**), 6.20 (bs, 2 H, D_2O exchangeable NH_2), 7.60 (s, 4 H, Ar−H), 7.94 (s, 0.6 H, CH═N **sp**), 8.15$_{(ap)}$ (s, 0.4 H, CH═N **ap**), 8.52, 8.54 (2 s, 1 H, D_2O exchangeable N(1)H **sp** + **ap**), 11.54, 11.65 (2 s, 1 H, D_2O exchangeable NH **sp** + **ap**), 11.95 (bs, 0.6 H, D_2O exchangeable NHAc). ^{13}C NMR (125 MHz, DMSO-d_6) δ ppm: 23.3 (CH_3), 32.3 (SCH_2 **sp**), 33.3 (SCH_2 **ap**), 95.2 (C-5 **sp**), 95.3 (C-5 **ap**), 123.6, 129.3, 129.4, 130.7, 132.3, 132.5, 133.8, 133.9 (Ar−C), 142.8 (CH═N **sp**), 146.3 (CH═N **ap**), 161.3 (C-2), 164.7 (C-6), 169.54, 169.59 (2 CO). Anal. Calc. for $C_{15}H_{15}BrN_6O_3S$: C, 41.01; H, 3.44; N, 19.13; S, 7.30. Found: C, 41.23; H, 3.27; N, 19.40; S, 7.24.

*5.1.3.3. (E)-N-(4-amino-2-((2-(2-(4-nitrobenzylidene)-hydrazinyl)-2-oxoethyl)thio)-6-oxo-1,6-dihydropyrimidin-5-yl)acetamide (**8**).* Yield 87%, mp 251−254 °C, R_F = 0.51 (CH_2Cl_2/ CH_3OH 4:1). ^1H NMR (500 MHz, DMSO-d_6) δ ppm: 1.61, 1.88 (2 s, 3 H, CH_3), 3.88 (s, 0.6 H, SCH_2 **ap**), 4.40 (s, 1.4 H, SCH_2 **sp**), 6.21 (bs, 2 H, D_2O exchangeable NH_2), 7.94 (d, 2 H, Ar−H), 8.07 (s, 0.6 H, CH═N **sp**), 8.29 (s, 0.4 H, CH═N **ap**), 8.24 (d, 2 H, J = 8.5 Hz, Ar−H), 8.52, 8.54 (2 s, 1 H, D_2O exchangeable N(1)H **sp** + **ap**), 11.78, 11.88 (2 s, 1 H, D_2O exchangeable NH **sp** + **ap**), 12.01 (bs, 1 H, D_2O exchangeable NHAc). ^{13}C NMR (125 MHz, DMSO-d_6) δ ppm: 23.3 (CH_3), 32.4 (SCH_2), 95.2 (C-5), 124.6, 128.4, 128.5, 140.88, 141.6 (Ar−C), 145.0, 148.2, 148.3 (CH═N **sp** + **ap**), 169.6, 169.9 (2 CO). Anal. Calc. for $C_{15}H_{15}N_7O_5S$: C, 44.44; H, 3.73; N, 24.19; S, 7.91. Found: C, 44.70; H, 3.54; N, 24.48; S, 8.05. HRMS (ESI) m/z Calcd For $C_{15}H_{15}N_7O_5S$ $[M + 1]^+$: 406.0934; found 406.0928.

*5.1.3.4. (E)-N-(4-amino-2-((2-(2-(4-methoxybenzylidene)-hydrazinyl)-2-oxoethyl)thio)-6-oxo-1,6-dihydropyrimidin-5-yl)acetamide (**9**).* Yield 76%, mp 245−247 °C, R_F = 0.56 (CH_2Cl_2/ CH_3OH 4:1). ^1H NMR (500 MHz, DMSO-d_6) δ ppm: 1.62, 1.88 (2 s, 3 H, CH_3), 3.75 (s, 3 H, OCH_3), 3.82 (s, 0.6 H, SCH_2 **ap**), 4.34 (s, 1.4 H, SCH_2 **sp**), 6.21 (bs, 2 H, D_2O exchangeable NH_2), 6.96 (d, 2 H, J = 8.5 Hz Ar−H), 7.58 (t, 2 H, Ar−H), 7.91 (s, 0.6 H, CH═N **sp**), 8.11 (s, 0.4 H, CH═N **ap**), 8.52, 8.55 (2 s, 1 H, D_2O exchangeable N(1)H **sp** + **ap**) 11.34, 11.47 (2 s, 1 H, D_2O exchangeable NH **sp** + **ap**), 11.96 (bs, 1 H, D_2O exchangeable NHAc). ^{13}C NMR (125 MHz, DMSO-d_6) δ ppm: 23.3 (CH_3), 32.4 (SCH_2 **sp**), 33.3 (SCH_2 **ap**), 55.8 (OCH_3), 95.2 (C-5 **sp**), 95.3 (C-5 **ap**), 114.8, 127.1, 129.0, 129.2 (Ar−C), 143.8 (CH═N **sp**), 147.4 (CH═N **ap**), 161.1 (C-4), 161.3 (C-2), 164.3 (C-6), 169.2, 169.5 (2 CO). Anal. Calc. for $C_{16}H_{18}N_6O_4S$: C, 49.22; H, 4.65; N, 21.53; S, 8.21. Found: C, 49.49; H, 4.81; N, 21.62; S, 8.35.

*5.1.3.5. (E)-N-(4-amino-2-((2-(2-(2-hydroxybenzylidene)-hydrazinyl)-2-oxoethyl)thio)-6-oxo-1,6-dihydropyrimidin-5-yl)acetamide (**10**).* Yield 81%, mp 244−246 °C, R_F = 0.46 (CH_2Cl_2/ CH_3OH 4:1). ^1H NMR (500 MHz, DMSO-d_6) δ ppm: 1.62, 1.88 (2 s, 3 H, CH_3), 3.86 (s, 0.95 H, SCH_2 **ap**), 4.33 (s, 0.85 H, SCH_2 **sp**), 6.19 (bs, 2 H, D_2O exchangeable NH_2), 6.82−6.87 (m, 2 H, Ar−H), 7.18−7.25 (m, 1 H, Ar−H), 7.49, 7.67 (2 d, 1 H, Ar−H), 8.27, 8.40 (2 s, 1 H, CH═N **sp** + **ap**), 8.51, 8.55 (2 s, 1 H, D_2O exchangeable N(1)H **sp** + **ap**), 10.04, 10.95 (2 s, 1 H, D_2O exchangeable OH **sp** + **ap**), 11.52, 11.67 (2 s, 1 H, D_2O exchangeable NH **sp** + **ap**), 11.98 (bs, 1 H, D_2O exchangeable NHAc). ^{13}C NMR (125 MHz, DMSO-d_6) δ ppm: 23.3 (CH_3), 32.4 (SCH_2 **sp**), 33.1 (SCH_2 **ap**), 95.2, 95.3 (C-5 **sp** + **ap**), 116.6, 116.8, 119.1, 119.8, 120.0, 120.5, 126.8, 129.6, 131.7, 131.9 (Ar−C), 141.4 (CH═N **sp**), 147.6 (CH═N **ap**), 156.8 (C-4), 157.7 (C-2), 164.4 (C-6), 169.1, 169.5 (2 CO). Anal. Calc. for $C_{15}H_{16}N_6O_4S$: C, 47.87; H, 4.28; N, 22.33; S, 8.52. Found: C, 47.96; H, 4.16; N, 22.51; S, 8.64. HRMS (ESI) m/z Calcd For $C_{15}H_{16}N_6O_4S$ $[M + 1]^+$: 377.1032; found 377.1030.

*5.1.4. Synthesis of 1,2,4-triazolo[4,3-a]pyrimidin-5(1H)-one Derivatives (**14**−**21**). 5.1.4.1. 3,7-Dimethyl-1,2,4-triazolo[4,3-a]pyrimidin-5(1H)-one (**14**).* 2-Hydrazinyl-6-methylpyrimidin-4-one **13** (0.5 g, 3.6 mmol) was heated in acetic acid (3 mL) under reflux for 9 h. The crude product precipitated was filtered off, washed with ether and dried, recrystallized from absolute ethanol; yield 76%; mp 300−302 °C (Lit. m. p.[48] 302−304 °C),. R_F = 0.53 (CH_2Cl_2/ CH_3OH 9:1). ^1H NMR (500 MHz, DMSO-d_6) δ ppm: 2.24 (s, 3 H, C(7)−CH_3), 2.70 (s, 3 H, C(3)−CH_3), 5.56 (s, 1 H, H-6), 13.22 (bs, 1 H, D_2O exchangeable NH). ^{13}C NMR (125 MHz, DMSO-d_6) δ ppm: 13.7 (C(3)-$\underline{C}H_3$), 19.9 (C(7)-$\underline{C}H_3$), 99.9 (C-6), 143.7 (C-7),156.4 (C-9),157.9 (C-3), 165.1 (C = O).

*5.1.4.2. Methyl 2-(3,7-dimethyl-5-oxo-1,2,4-triazolo[4,3-a]pyrimidin-1(5H)-yl)acetate (**15**).* Compound **14** (0.31 g, 1.9 mmol) was stirred for 20 min with anhydrous potassium carbonate (0.33 g, 2.3 mmol) in acetone (35 mL); then ethyl bromoacetate (0.3 mL, 2.7 mmol) was added to the reaction mixture and continue stirring for 24 h at room temperature. The mixture was filtered off and evaporated under diminished pressure. The crude obtained was recrystallized from methanol as colorless crystals in 85% yield; mp 143−145 °C, R_F = 0.6 (CH_2Cl_2/ CH_3OH 9.5:0.5). ^1H NMR (500 MHz, DMSO-d_6) δ ppm: 2.29 (s, 3 H, C(7)−CH_3), 2.83 (s, 3 H, C(3)−CH_3), 3.78 (s, 3 H, OCH_3), 4.93 (s, 2 H, NCH_2), 5.79 (s, 1 H, H-6). ^{13}C NMR (125 MHz, DMSO-d_6) δ ppm: 13.9 (C(3)-$\underline{C}H_3$), 23.7 (C(7)-$\underline{C}H_3$), 31.0 (OCH_3), 48.0 (NCH_2), 100.4 (C-6), 143.6 (C-7), 149.4 (C-9), 157.5 (C-3), 165.8 (C-5), 166.9 ($\underline{C}OOCH_3$). Anal. Calc. for $C_{10}H_{12}N_4O_3$: C, 50.48; H, 5.12; N, 23.72. Found: C, 51.18; H, 5.37; N, 23.95.

*5.1.4.3. 2-(3,7-Dimethyl-5-oxo-1,2,4-triazolo[4,3-a]-pyrimidin-1(5H)-yl)acetohydrazide (**16**).* A mixture of **15** (0.5 g, 2 mmol) and hydrazine hydrate (4 mL, 82 mmol) in ethanol (30 mL) was refluxed for 4 h. The white precipitate formed was filtered off, washed with ethanol, and dried. Recrystallized from ethanol/H_2O to give **16** as a white powder in 85% yield; mp decomp. > 260 °C, R_F = 0.43 (CH_2Cl_2/ CH_3OH 9:1). ^1H NMR (500 MHz, DMSO-d_6) δ ppm: 2.17, 2.18 (2 s, 3 H, C(7)−CH_3 **sp, ap**), 2.66, 2.68 (2 s, 3 H, C(3)−CH_3 **sp, ap**), 4.30 (s, 1.8 H, D_2O exchangeable NH_2 **sp**), 4.56 (s, 0.2 H, D_2O exchangeable NH_2 **ap**), 4.67 (s, 1.8 H, NCH_2 **sp**), 5.02 (s, 0.2 H, NCH_2 **ap**), 5.66, 5.68 (2 s, 1 H, H-6 **sp, ap**), 8.79 (s, 0.1 H, D_2O exchangeable NH **ap**), 9.23 (s, 0.9 H, D_2O exchangeable NH **sp**). ^{13}C NMR (125 MHz, DMSO-d_6) δ ppm: 13.9 (C(3)-$\underline{C}H_3$), 24.5 (C(7)-$\underline{C}H_3$), 47.8 (NCH_2 **ap**), 47.9 (NCH_2 **sp**), 98.6 (C-6 **ap**), 98.9 (C-6 **sp**), 142.0 (C-7 **ap**), 142.6 (C-7 **sp**), 150.4 (C-9 **sp**), 150.6 (C-9 **ap**), 157.7 (C-3 **ap**), 157.8 (C-3 **sp**), 165.2, 167.2, 167.3, 169.4 (2 CO **sp, ap**). Anal. Calc. for $C_9H_{12}N_6O_2$: C, 45.76; H, 5.12; N, 35.58. Found: C, 45.99; H, 5.30; N, 35.82.

*5.1.5. General Procedure for the Preparation (E)-N′-(substitutedbenzylidene)-2-(3,7-dimethyl-5-oxo-1,2,4-triazolo[4,3-a]pyrimidin-1(5H)-yl)acetohydrazide (**17**−**21**).* Compound **16** (1 mmol) and different aromatic aldehydes (1 mmol) were refluxed in ethanol (30 mL) for 2−4 h, and few drops of glacial acetic acid (2−3 drops) were added as a catalyst, to afford the corresponding *N′*-(substitutedbenzylidene)-acetohydrazides **17**−**21,** and recrystallized from pure ethanol.

5.1.5.1. (E)-N′-(4-chlorobenzylidene)-2-(3,7-dimethyl-5-oxo-1,2,4-triazolo[4,3-a]pyrimidin-1(5H)-yl)acetohydrazide

https://doi.org/10.1021/acsomega.4c00466
ACS Omega 2024, 9, 21042−21057

*(**17**)*. Yield 91%, mp 237−240 °C, R_F = 0.49 (ethyl acetate). ^{1}H NMR (500 MHz, DMSO-d_6) δ ppm: 2.17, 2.18 (2 s, 3 H, C(7)−CH_3 **sp** + **ap**), 2.69, 2.70 (s, 3 H, C(3)−CH_3 **sp** + **ap**), 4.90 (s, 0.5 H, CH_2 **ap**), 5.30 (s, 1.5 H, CH_2 **sp**), 5.70, 5.71 (2 s, 1 H, H-6 **sp** + **ap**), 7.46, 7.48 (2 d, 2 H, J = 8 Hz, Ar−H **sp** + **ap**), 7.69, 7.72 (2 d, 2 H, Ar−H **sp** + **ap**), 7.97 (s, 0.75 H, CH═N **sp**), 8.17 (s, 0.25 H, CH═N **ap**), 11.80, 11.88 (2 s, 1 H, D_2O exchangeable NH **sp** + **ap**). ^{13}C NMR (125 MHz, DMSO-d_6) δ ppm: 13.9 (C(3)-$\underline{C}H_3$), 24.5 (C(7)-$\underline{C}H_3$), 48.1 (NCH_2 **sp**), 48.4 (NCH_2 **ap**), 99.0 (C-6 **sp**), 99.1 (C-6 **ap**), 129.2, 129.4 (Ar−C), 133.2 (Ar−C-1' **sp**), 133.3 (Ar−C-1' **ap**), 135.1 (Ar−C-4' **sp**), 135.2 (Ar−C-4' **ap**), 142.3(C-3 **sp**), 142.6 (C-3 **ap**), 143.9 (CH═N **sp**), 147.1 (CH═N **ap**), 150.5 (C-9 **ap**), 150.6 (C-9 **sp**), 157.71 (C-7 **sp**), 157.75 (C-7 **ap**), 162.7 (CONH **ap**), 167.4 (CONH **sp**), 167.5 (C-5). Anal. Calc. for $C_{16}H_{15}ClN_6O_2$: C, 53.56; H, 4.21; N, 23.42. Found: C, 53.78; H, 4.39; N, 23.70.

*5.1.5.2. (E)-N′-(4-bromobenzylidene)-2-(3,7-dimethyl-5-oxo-1,2,4-triazolo[4,3-a]pyrimidin-1(5H)-yl)acetohydrazide (**18**)*. Yield 71%, mp 252−255 °C, R_F = 0.57 (ethyl acetate). ^{1}H NMR (500 MHz, DMSO-d_6) δ ppm: 2.17, 2.18 (2 s, 3 H, C(7)−CH_3 **sp** + **ap**), 2.70 (s, 3 H, C(3)−CH_3), 4.89 (s, 0.5 H, NCH_2 **ap**), 5.30 (s, 1.5 H, NCH_2 **sp**), 5.70, 5.71 (2 s, 1 H, H-6 **sp** + **ap**), 7.58−7.65 (m, 4 H, Ar−H), 7.95 (s, 0.75 H, CH═N **sp**), 8.15 (s, 0.25 H, CH═N **ap**), 11.87 (bs, 1 H, D_2O exchangeable NH). ^{13}C NMR (125 MHz, DMSO-d_6) δ ppm: 13.9 (C(3)-$\underline{C}H_3$), 24.5 (C(7)-$\underline{C}H_3$), 48.1 (NCH_2 **sp**), 48.4 (NCH_2 **ap**), 99.0 (C-6 **sp**), 99.1 (C-6 **ap**), 123.9, 124.1, 129.54, 129.5, 132.3, 132.4, 133.5, 133.6 (Ar−C), 142.3 (C-3 **sp**), 142.6 (C-3 **ap**), 144.0 (CH═N **sp**), 147.2 (CH═N **ap**), 150.5 (C-9 **ap**), 150.6 (C-9 **sp**), 157.7 (C-7 **sp**), 157.74 (C-7 **ap**), 162.7 (CONH **ap**), 167.4 (CONH **sp**), 167.5 (C-5). Anal. Calc. for $C_{16}H_{15}BrN_6O_2$: C, 47.66; H, 3.75; N, 20.84. Found: C, 47.90; H, 3.87; N, 21.09. HRMS (ESI) m/z Calcd For $C_{16}H_{15}BrN_6O_2$ $[M + 1]^+$: 403.0518; found 403.0516.

*5.1.5.3. (E)-N′-(4-nitrobenzylidene)-2-(3,7-dimethyl-5-oxo-1,2,4-triazolo[4,3-a]pyrimidin-1(5H)-yl)acetohydrazide (**19**)*. Yield 96%, mp 254−255 °C, R_F = 0.41 (ethyl acetate). ^{1}H NMR (500 MHz, DMSO-d_6) δ ppm: 2.17, 2.18 (2 s, 3 H, C(7)−CH_3 **sp** + **ap**), 2.70 (s, 3 H, C(3)−CH_3), 4.94 (s, 0.5 H, NCH_2 **ap**), 5.35 (2 s, 1.5 H, NCH_2 **sp**), 5.69, 5.71 (2 s, 1 H, H-6 **sp** + **ap**), 7.93, 7.96 (2 d, 2 H, J = 8.5 Hz, Ar−H **sp** + **ap**), 8.08 (s, 0.78 H, CH═N **sp**), 8.23, 8.25 (2 d, 2 H, Ar−H **sp** + **ap**), 8.28 (s, 0.22 H, CH═N **ap**), 12.10 (bs, 1 H, D_2O exchangeable NH). ^{13}C NMR (125 MHz, DMSO-d_6) δ ppm: 13.9 (C(3)-$\underline{C}H_3$), 24.5 (C(7)-$\underline{C}H_3$), 48.1 (NCH_2 **sp**), 48.5 (NCH_2 **ap**), 99.0 (C-6 **sp**), 99.1 (C-6 **ap**), 124.4, 124.5, 128.5, 128.7, 140.5 (Ar−C), 142.4 (C-3), 142.9 (CH═N **sp**), 148.3 (CH═N **ap**), 146.0 (Ar−C−NO_2), 150.5 (C-9 **ap**), 150.6 (C-9 **sp**), 157.7 (C-7), 163.1 (CONH **ap**), 167.4 (CONH **sp**), 167.9 (C-5). Anal. Calc. for $C_{16}H_{15}N_7O_4$: C, 52.03; H, 4.09; N, 26.55. Found: C, 52.30; H, 4.21; N, 26.64.

*5.1.5.4. (E)-N′-(4-methoxybenzylidene)-2-(3,7-dimethyl-5-oxo-1,2,4-triazolo[4,3-a]pyrimidin-1(5H)-yl)acetohydrazide (**20**)*. Yield 97%, mp 265−267 °C, R_F = 0.46 (ethyl acetate). ^{1}H NMR (500 MHz, DMSO-d_6) δ ppm: 2.18, 2.19 (2 s, 3 H, C(7)−CH_3 **sp** + **ap**), 2.70 (s, 3 H, C(3)−CH_3), 3.75 (s, 3 H, OCH_3) 4.86 (s, 0.5 H, NCH_2 **ap**), 5.26 (s, 1.5 H, NCH_2 **sp**), 5.70, 5.71 (2 s, 1 H, H-6 **sp** + **ap**), 6.95 (d, 2 H, J = 8.5 Hz, Ar−H), 7.62 (d, 2 H, Ar−H), 7.92 (s, 0.75 H, CH═N **sp**), 8.11 (s, 0.25 H, CH═N **ap**), 11.69 (bs, 1 H, D_2O exchangeable NH). ^{13}C NMR (125 MHz, DMSO-d_6) δ ppm: 13.9 (C(3)-$\underline{C}H_3$), 24.5 (C(7)-$\underline{C}H_3$), 48.1 (NCH_2 **sp**), 48.4 (NCH_2 **ap**), 55.8 (OCH_3), 98.9 (C-6 **sp**), 99.1 (C-6 **ap**), 114.7, 114.8, 126.8, 126.9, 129.1, 129.3 (Ar−C), 142.3 (C-3 **sp**), 142.5 (C-3 **ap**), 145.1 (CH═N **sp**), 148.3 (CH═N **ap**), 150.5 (C-9 **ap**), 150.6 (C-9 **sp**), 157.7 (C-7 **sp**), 157.8 (C-7 **ap**), 161.3 (C-5 **ap**), 162.2 (CONH **ap**), 167.1 (CONH **sp**), 167.3 (C-5 **sp**). Anal. Calc. for $C_{17}H_{18}N_6O_3$: C, 57.62; H, 5.12; N, 23.72. Found: C, 57.89; H, 5.36; N, 23.98.

*5.1.5.5. (E)-N′-(2-hydroxybenzylidene)-2-(3,7-dimethyl-5-oxo-1,2,4-triazolo[4,3-a]pyrimidin-1(5H)-yl)acetohydrazide (**21**)*. Yield 83%, mp 250−252 °C, R_F = 0.50 (ethyl acetate). ^{1}H NMR (500 MHz, DMSO-d_6) δ ppm: 2.18, 2.19 (s, 3 H, C(7)−CH_3 **sp** + **ap**), 2.70 (s, 3 H, C(3)−CH_3), 4.91 (s, 0.8 H, NCH_2 **ap**), 5.27 (s, 1.2 H, NCH_2 **sp**), 5.69, 5.71 (2 s, 1 H, H-6 **sp** + **ap**), 6.80 (t, 1 H, Ar−H), 6.84−6.87 (m, 1 H, Ar−H), 7.18−7.26 (m, 1 H, Ar−H), 7.51, 7.52 (dd, 0.4 H, Ar−H **ap**, J = 1.5 Hz), 7.70 (dd, 0.6 H, J = 7.5 Hz, Ar−H **sp**), 8.30 (s, 0.6 H, CH═N **sp**), 8.40 (s, 0.4 H, CH═N **ap**), 10.03, 10.85 (2 bs, 0.5 H, D_2O exchangeable, Ar−OH **sp** + **ap**), 11.74 (bs, 1 H, D_2O exchangeable, NH). ^{13}C NMR (125 MHz, DMSO-d_6) δ ppm: 13.9 (C(3)-$\underline{C}H_3$), 24.5 (C(7)−CH_3), 48.1 (NCH_2 **sp**), 48.3 (NCH_2 **ap**), 98.9 (C-6 **sp**), 99.1 (C-6 **ap**), 116.6, 116.8, 119.1, 119.8, 120.4, 126.6, 129.4, 131.9, 132.1 (Ar−C), 142.2 (C-3 **sp**), 142.7 (C-3 **ap**), 142.3 (CH═N **sp**), 148.3 (CH═N **ap**), 150.5 (C-9 **ap**), 150.6 (C-9 **sp**), 156.9 (C-7 **sp**), 157.7 (C-7 **ap**), 162.4 (CONH **ap**), 167.1 (CONH **sp**), 167.3 (C-5). Anal. Calc. for $C_{16}H_{16}N_6O_3$: C, 56.47; H 4.74; N 24.69. Found: C, 56.79; H, 4.85; N, 24.94. HRMS (ESI) m/z Calcd For $C_{16}H_{16}N_6O_3$ $[M + 1]^+$: 341.1362; found 341.1360.

5.2. X-ray Structure Determinations. The details of solving the crystal structure of **15** are described in Supporting Information.[49−52] The crystallographic details are summarized in Tables S1−3.

5.3. Biological Assays. *5.3.1. MTT Assay.* The cytotoxicity of the studied compounds against normal and breast cancer cell lines was tested using MTT assay[40] as detailed in the Supporting Information.

5.3.2. DNA Binding Studies. Materials and fluorescence measurements are detailed in the Supporting Information.

5.3.3. CDK-2 Inhibition. The CDK2 enzyme inhibitory activity was performed by using the CDK2/CyclinA2 Kinase Enzyme System (catalog No. V2971) (Promega, Milan, Italy), according to the manufacturer's instructions.

5.4. Docking and Molecular Dynamics Simulations. The 3D crystal structures of the DNA dodecamer cocrystallized with distamycin and were retrieved from the Protein Data Bank (PDB, www.rcsb.org) PDB ID: 2DND[45,47] respectively. After protein preparation procedure, docking of the energy minimized for the pyrimidine derivatives **5** and **8** was performed employing MOE 2019.102[46] as detailed in the Supporting Information. To get further insights into the 2FVD-8 protein−ligand interaction stability, molecular dynamics (MD) calculations were carried out on the best docking pose. The input files for MD calculations were generated using CHARMM-GUI solution builder using CHARMM force field parameters for protein. The topology of the ligands was generated by CHARMM General Force field through Param-Chem server. GROMACS 2020.2 software was used to carry out the MD simulation. Trajectory analysis and binding free energy (MM/PBSA calculations) are detailed in the Supporting Information.

5.5. Apoptosis Studies. The induced apoptosis/necrosis by the test compounds was determined using Annexin V-FITC/PI double staining. MCF-7 cells (3×10^5/well) were plated in 6-well plates and cultured overnight, treated with IC_{50} of the tested compounds. The cells were harvested and treated as mentioned in the Supporting Information.

https://doi.org/10.1021/acsomega.4c00466
ACS Omega 2024, 9, 21042−21057

5.6. Statistical Analysis. The data representation and analysis were performed as detailed in the Supporting Information.

■ ASSOCIATED CONTENT

Supporting Information

The Supporting Information is available free of charge at https://pubs.acs.org/doi/10.1021/acsomega.4c00466.

All spectral analysis results as well as X-ray detailed tables and information are included. In addition, detailed biological analysis methods are explained (PDF)

■ AUTHOR INFORMATION

Corresponding Authors

Laila F. Awad − *Chemistry Department, Faculty of Science, Alexandria University, Alexandria 21321, Egypt;* orcid.org/0000-0001-9521-5511; Email: laila.fathy@yahoo.com

Assem Barakat − *Department of Chemistry, College of Science, King Saud University, Riyadh 11451, Saudi Arabia;* orcid.org/0000-0002-7885-3201; Email: ambarakat@ksu.edu.sa

Authors

Mohamed N. Abd Al Moaty − *Chemistry Department, Faculty of Science, Alexandria University, Alexandria 21321, Egypt;* orcid.org/0000-0003-2843-9704

Yeldez El Kilany − *Chemistry Department, Faculty of Science, Alexandria University, Alexandria 21321, Egypt*

Saied M. Soliman − *Chemistry Department, Faculty of Science, Alexandria University, Alexandria 21321, Egypt;* orcid.org/0000-0001-8405-8370

Nihal A. Ibrahim − *Chemistry Department, Faculty of Science, Alexandria University, Alexandria 21321, Egypt*

Marwa M. Abu-Serie − *Medical Biotechnology Department, Genetic Engineering and Biotechnology Research Institute, City of Scientific Research and Technological Applications (SRTA-City), Alexandria 21934, Egypt*

Matti Haukka − *Department of Chemistry, University of Jyväskylä, FI-40014 Jyväskylä, Finland;* orcid.org/0000-0002-6744-7208

Amira El-Yazbi − *Department of Pharmaceutical Analytical Chemistry, Faculty of Pharmacy, Alexandria University, Alexandria 21521, Egypt;* orcid.org/0000-0002-1717-5291

Mohamed Teleb − *Department of Pharmaceutical Chemistry, Faculty of Pharmacy, Alexandria University, Alexandria 21521, Egypt*

Complete contact information is available at: https://pubs.acs.org/10.1021/acsomega.4c00466

Notes

The authors declare no competing financial interest.

■ ACKNOWLEDGMENTS

The author would like to extend their sincere appreciation to the Researchers Supporting Project (RSP2024R64), King Saud University, Riyadh, Saudi Arabia.

■ REFERENCES

(1) Bray, F.; Ferlay, J.; Soerjomataram, I.; Siegel, R.; Torre, L.; Jemal, A. Erratum: Global cancer statistics 2018: GLOBOCAN estimates of incidence and mortality worldwide for 36 cancers in 185 countries. *Cancer J. Clin.* **2020**, *70*, 313.

(2) Siegel, R. L.; Miller, K. D.; Jmal, A. Cancer statistics, 2020. *Cancer J. Clin.* **2020**, *70*, 7−30.

(3) Lee, J. E.; Lee, S. A.; Kim, T. H.; Park, S.; Choy, Y. S.; Ju, Y. J.; Park, E.-C. Projection of breast cancer burden due to reproductive/lifestyle changes in Korean women (2013−2030) using an age-period-cohort model. *Cancer Res. Treat.* **2018**, *50*, 1388−1395.

(4) Quante, A. S.; Ming, C.; Rottmann, M.; Engel, J.; Boeck, S.; Heinemann, V.; Westphalen, C. B.; Strauch, K. Projections of cancer incidence and cancer-related deaths in Germany by 2020 and 2030. *Cancer Med.* **2016**, *5*, 2649−2656.

(5) Falzone, L.; Salomone, S.; Libra, M. Evolution of cancer pharmacological treatments at the turn of the third millennium. *Front. Pharmacol.* **2018**, *9*, 1300.

(6) Xie, Y.-H.; Chen, Y.-X.; Fang, J.-Y. Comprehensive review of targeted therapy for colorectal cancer. *Signal Transduction Targeted Ther.* **2020**, *5* (1), 22.

(7) Fisusi, F. A.; Akala, E. O. Drug combinations in breast cancer therapy. *Pharm. Nanotechnol.* **2019**, *7*, 3−23.

(8) Meunier, B. Hybrid molecules with a dual mode of action: dream or reality? *Acc. Chem. Res.* **2008**, *41*, 69−77.

(9) Norouzi, P.; Motasadizadeh, H.; Atyabi, F.; Dinarvand, R.; Gholami, M.; Farokhi, M.; Shokrgozar, M. A.; Mottaghitalab, F. Combination therapy of breast cancer by codelivery of doxorubicin and survivin siRNA using polyethylenimine modified silk fibroin nanoparticles. *ACS Biomater. Sci. Eng.* **2021**, *7*, 1074−1087.

(10) Watson, J. D.; Crick, F. H. Molecular structure of nucleic acids: a structure for deoxyribose nucleic acid. *Nature* **1953**, *171*, 737−738.

(11) Arlin, Z. A. Current status of amsacrine (AMSA) combination chemotherapy programs in acute leukemia. *Cancer Treat. Rep.* **1983**, *67*, 967−970.

(12) Arcamone, F. Properties of antitumor anthracyclines and new developments in their application: Cain Memorial Award Lecture. *Cancer Res.* **1985**, *45* (12 Pt 1), 5995−5999.

(13) Gurova, K. New hopes from old drugs: revisiting DNA-binding small molecules as anticancer agents. *Future Oncol.* **2009**, *5*, 1685−1704.

(14) Mukherjee, A.; Sasikala, W. D. Drug−DNA intercalation: From discovery to the molecular mechanism. *Adv. Protein Chem. Struct. Biol.* **2013**, *92*, 1−62.

(15) Sharma, V.; Gupta, M.; Kumar, P.; Sharma, A. A Comprehensive Review on Fused Heterocyclic as DNA Intercalators: Promising Anticancer Agents. *Curr. Pharm. Des* **2021**, *27*, 15−42.

(16) Deans, A. J.; Khanna, K. K.; McNees, C. J.; Mercurio, C.; Heierhorst, J. R.; McArthur, G. A. Cyclin-dependent kinase 2 functions in normal DNA repair and is a therapeutic target in BRCA1-deficient cancers. *Cancer Res.* **2006**, *66*, 8219−8226.

(17) Senderowicz, A. M. Small-molecule cyclin-dependent kinase modulators. *Oncogene* **2003**, *22*, 6609−6620.

(18) Maggiorella, L.; Deutsch, E.; Frascogna, V.; Chavaudra, N.; Jeanson, L.; Milliat, F.; Eschwege, F. O.; Bourhis, J. Enhancement of radiation response by roscovitine in human breast carcinoma in vitro and in vivo. *Cancer Res.* **2003**, *63* (10), 2513−2517.

(19) Zhu, Y.; Alvarez, C.; Doll, R.; Kurata, H.; Schebye, X. M.; Parry, D.; Lees, E. Intra-S-phase checkpoint activation by direct CDK2 inhibition. *Mol. Cell. Biol.* **2004**, *24*, 6268−6277.

(20) Tetsu, O.; McCormick, F. Proliferation of cancer cells despite CDK2 inhibition. *Cancer Cell* **2003**, *3*, 233−245.

(21) Tadesse, S.; Anshabo, A. T.; Portman, N.; Lim, E.; Tilley, W.; Caldon, C. E.; Wang, S. Targeting CDK2 in cancer: challenges and opportunities for therapy. *Drug Discovery Today* **2020**, *25*, 406−413.

(22) Tadesse, S.; Caldon, E. C.; Tilley, W.; Wang, S. Cyclin-dependent kinase 2 inhibitors in cancer therapy: an update. *J. Med. Chem.* **2019**, *62*, 4233−4251.

(23) Mukhija, A. Influence of oxidative stress on drug-DNA binding: Microcalorimetric and mechanistic insights with anticancer drugs. *J. Mol. Liq.* **2022**, *368*, 120769.

(24) Coxon, C. R.; Anscombe, E.; Harnor, S. J.; Martin, M. P.; Carbain, B.; Golding, B. T.; Hardcastle, I. R.; Harlow, L. K.; Korolchuk, S.; Matheson, C. J. Cyclin-Dependent Kinase (CDK) Inhibitors: Structure−Activity Relationships and Insights into the CDK-2 Selectivity of 6-Substituted 2-Arylaminopurines. *J. Med. Chem.* **2017**, *60* (5), 1746−1767.
(25) Lan, H.; Song, J.; Yuan, J.; Xing, A.; Zeng, D.; Hao, Y.; Zhang, Z.; Feng, S. S. Biological Evaluation, DNA Binding, and Molecular Docking of Hybrid 4, 6-Dihydrazone Pyrimidine Derivatives as Antitumor Agents. *Molecules* **2022**, *28* (1), 187.
(26) Shaikh, A. S.; Kiranmai, G.; Devi, G. P.; Makhal, P. N.; Sigalapalli, D. K.; Tokala, R.; Kaki, V. R.; Shankaraiah, N.; Nagesh, N.; Babu, B. N. Exploration of mercaptoacetamide-linked pyrimidine-1, 3, 4-oxadiazole derivatives as DNA intercalative topo II inhibitors: Cytotoxicity and apoptosis induction. *Bioorg. Med. Chem. Lett.* **2022**, *65*, 128697.
(27) Tokala, R.; Mahajan, S.; Kiranmai, G.; Sigalapalli, D. K.; Sana, S.; John, S. E.; Nagesh, N.; Shankaraiah, N. Development of β-carboline-benzothiazole hybrids via carboxamide formation as cytotoxic agents: DNA intercalative topoisomerase IIα inhibition and apoptosis induction. *Bioorg. Chem.* **2021**, *106*, 104481.
(28) Fanta, B. S.; Mekonnen, L.; Basnet, S. K.; Teo, T.; Lenjisa, J.; Khair, N. Z.; Kou, L.; Tadesse, S.; Sykes, M. J.; Yu, M. 2-Anilino-4-(1-methyl-1H-pyrazol-4-yl) pyrimidine-derived CDK2 Inhibitors as Anticancer Agents: Design, Synthesis & Evaluation. *Bioorg. Med. Chem.* **2023**, *2023*, 117158.
(29) Jones, C. D.; Andrews, D. M.; Barker, A. J.; Blades, K.; Daunt, P.; East, S.; Geh, C.; Graham, M. A.; Johnson, K. M.; Loddick, S. A. The discovery of AZD5597, a potent imidazole pyrimidine amide CDK inhibitor suitable for intravenous dosing. *Bioorg. Med. Chem. Lett.* **2008**, *18* (24), 6369−6373.
(30) El-Yazbi, A. F.; El-Kimary, I. Novel inexpensive 'turn-on'fluorescent biosensor for the sensitive detection of DNA damage induced by epirubicin. *Microchem. J.* **2021**, *168*, 106535.
(31) El-Yazbi, A. F.; Khalil, H. A.; Belal, T. S.; El-Kimary, I. Inexpensive bioluminescent genosensor for sensitive determination of DNA damage induced by some commonly used sunscreens. *Anal. Biochem.* **2022**, *651*, 114700.
(32) Abraham, R. T. Cell cycle checkpoint signaling through the ATM and ATR kinases. *Genes Dev.* **2001**, *15*, 2177−2196.
(33) Satyanarayana, A.; Kaldis, P. A dual role of Cdk2 in DNA damage response. *Cell Div.* **2009**, *4* (1), 1−4.
(34) El Ashry, E. S. H.; Awad, L. F.; Teleb, M.; Ibrahim, N. A.; Abu-Serie, M. M.; Abd Al Moaty, M. N. Structure-based design and optimization of pyrimidine-and 1, 2, 4-triazolo [4, 3-a] pyrimidine-based matrix metalloproteinase-10/13 inhibitors via Dimroth rearrangement towards targeted polypharmacology. *Bioorg. Chem.* **2020**, *96*, 103616.
(35) Wieczorkiewicz, P. A.; Krygowski, T. M.; Szatylowicz, H. Intramolecular Interactions in Derivatives of Uracil Tautomers. *Molecules* **2022**, *27*, 7240.
(36) El Ashry, H.; Awad, L. F.; Nasr, M.; Kassem, A. A.; Soliman, S. M.; Zakaria, M. Synthesis, characterizations and conformational analysis of some new 2-arylidene N-(1, 3-dioxoisoindolin-2-yl) aminothiocarbohydrazides and their conversion to functionalized hybrids of isoindole core with thiadiazoline. *J. Mol. Struct.* **2021**, *1245*, 131230.
(37) Munir, R.; Javid, N.; Zia-Ur-Rehman, M.; Zaheer, M.; Huma, R.; Roohi, A.; Athar, M. M. Synthesis of novel N-acylhydrazones and their CN/NN bond conformational characterization by NMR spectroscopy. *Molecules* **2021**, *26*, 4908.
(38) Reis, D. C.; Despaigne, A. A. R.; Silva, J. G. D.; Silva, N. F.; Vilela, C. F.; Mendes, I. C.; Takahashi, J. A.; Beraldo, H. Structural studies and investigation on the activity of imidazole-derived thiosemicarbazones and hydrazones against crop-related fungi. *Molecules* **2013**, *18*, 12645−12662.
(39) El Ashry, E. S. H.; Awad, L. F.; Badawy, M. E.; Rabea, E. I.; Ibrahim, N. A.; Abd Al Moaty, M. N. Synthesis, antibacterial, antioxidant, and molecular docking studies of 6-methylpyrimidin-4 (3H)-one and oxo-1, 2, 4-triazolo [4, 3-a] pyrimidine derivatives. *J. Mol. Struct.* **2022**, *1249*, 131551.
(40) Mosmann, T. Rapid colorimetric assay for cellular growth and survival: application to proliferation and cytotoxicity assays. *J. Immunol. Methods* **1983**, *65*, 55−63.
(41) El-Yazbi, A. F.; Loppnow, G. R. Chimeric RNA−DNA molecular beacons for quantification of nucleic acids, single nucleotide polymophisms, and nucleic acid damage. *Anal. Chem.* **2013**, *85*, 4321−4327.
(42) El-Yazbi, A. F.; Loppnow, G. R. Probing DNA damage induced by common antiviral agents using multiple analytical techniques. *J. Pharm. Biomed. Anal.* **2018**, *157*, 226−234.
(43) Nair, S.; Hainer, A.; El-Yazbi, A. F. Two novel "release-on-demand" fluorescent biosensors for probing UV-induced DNA damage induced in single stranded and double stranded DNA: Comparative study. *Int. J. Biol. Macromol.* **2022**, *215*, 657−664.
(44) El-Yazbi, A. F.; Wong, A.; Loppnow, G. R. A luminescent probe of mismatched DNA hybridization: Location and number of mismatches. *Anal. Chim. Acta* **2017**, *994*, 92−99.
(45) Coll, M.; Frederick, C. A.; Wang, A.; Rich, A. A bifurcated hydrogen-bonded conformation in the d (AT) base pairs of the DNA dodecamer d (CGCAAATTTGCG) and its complex with distamycin. *Proc. Natl. Acad. Sci. U. S. A.* **1987**, *84*, 8385−8389.
(46) Chemical Computing Group, Inc Molecular Operating Environment [(MOE 2019.10); Chemical Computing Group Inc.; Montreal, QC, Canada, http://www.chemcomp.com (accessed 21 October 2023).
(47) Chu, X.-J.; DePinto, W.; Bartkovitz, D.; So, S.-S.; Vu, B. T.; Packman, K.; Lukacs, C.; Ding, Q.; Jiang, N.; Wang, K. Discovery of [4-amino-2-(1-methanesulfonylpiperidin-4-ylamino) pyrimidin-5-yl](2, 3-difluoro-6-methoxyphenyl) methanone (R547), a potent and selective cyclin-dependent kinase inhibitor with significant in vivo antitumor activity. *J. Med. Chem.* **2006**, *49* (22), 6549−6560.
(48) Golovinsky, E. Über das Verhalten einiger Orotsäure-Analoga und -Derivate unter den Bedingungen der Tsuji -Reaktion. *Z. Chem.* **1968**, *8* (11), 421.
(49) Oxoford, R. *DiffractionCrysAlisPro*; Agilent Technologies inc: Oxfordshire, England, Yarnton, 2018.
(50) Sheldrick, G. M. SHELXT−Integrated space-group and crystal-structure determination. *Acta Crystallogr., Sect. A: Found. Adv.* **2015**, *71*, 3−8.
(51) Sheldrick, G. M. Crystal structure refinement with SHELXL. *Acta Crystallogr., Sect. C: Struct. Chem.* **2015**, *71*, 3−8.
(52) Hübschle, C. B.; Sheldrick, G. M.; Dittrich, B. ShelXle: a Qt graphical user interface for SHELXL. *J. Appl. Crystallogr.* **2011**, *44*, 1281−1284.

https://doi.org/10.1021/acsomega.4c00466
ACS Omega 2024, 9, 21042−21057